Media and Motion
Research Implementation

Amal Alphonse
Simon Bignold
Yuchen Pei

May 2012

MASDOC
Mathematics and Statistics
Centre for Doctoral Training

Acknowledgements

Contents

List of Figures

1 Introduction

1.1 Motivation

Our paper is motivated by the mechanics of the heart. During normal heart activity, the heart pulsates at a regular rhythm. However, if heart tissue is damaged then the heart rhythm can become irregular: this is called an *arrhythmia*. These arrhythmias may be caused by changed electro-dynamical properties due to damaged heart tissue. This can potentially be fatal, so understanding such regimes is important.

The heart is in essence a pump and its primary function is to pump blood about the body. To this end, it expands to draw blood into the heart and contracts to push the blood around the body. The heart is split into two halves (see Figure 1): one half takes in de-oxygenated blood from the body and pumps it to the lungs where it is oxygenated, and the other half takes the oxygenated blood from the lungs and pumps it to the rest of the body. Each half of the heart has two chambers: the atrium which the blood flows into and the ventricle from which the blood is pumped out of. The
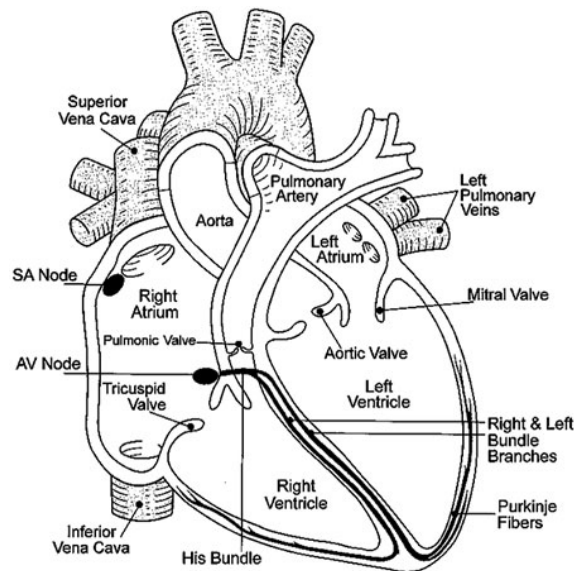
Figure 1: The heart (from [1])

contraction of the heart's chambers is caused by the contraction of the cells that line the chambers. The contraction is in turn activated by the arrival of the action potential. The action potential (see Figure 2 for a graph of a typical action potential and see [12, p. 15] for a more detailed picture) takes a certain amount of time to dissipate due to the electro-dynamical properties of the cell. In normal heart activity a pulse of the action potential travels from one end of a heart chamber to the other end and then dies out. In an arrhythmia, however, the pulsation becomes disturbed which can be caused by the generation of (re-entrant) spiral waves or turbulence. These spiral waves are dangerous since they affect the normal functioning of the heart and so it is a worthwhile task to study and understand the propagation of spiral waves. A much more detailed description of the biology of the heart can be found at the start of [12].

Our aims Given our time constraints, we will concentrate on simulating spiral waves on different surfaces. Specifically, we aim to

- create spiral waves on a 2D plane using both the finite element (FE) and finite difference (FD) methods
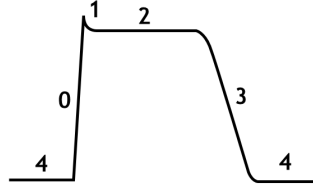
Figure 2: The action potential (from [17])

- create spiral waves on a static unit sphere and static ellipsoid

- create spiral waves on moving surfaces with a range of different magnitudes of oscillation and compare to the static case

- simulate inhomogeneities (surface holes and areas of reduced conductivity) in the sphere.

1.2 The Barkley Model

The heart can be modelled as an excitable system: the contraction of the heart is caused by the action potential exceeding a certain threshold, and the heart returns to a resting state afterwards. The well-studied FitzHugh–Nagumo model (and its forebear, the Hodgkin–Huxley model) is perhaps the prototypical choice to describe the action potential, however we choose to study a different but similar model (more information on different models can be found in [12]). To simulate the formation of spiral waves we use a coupled system of partial differential equations (PDEs) that lie on a surface Γ:

$$\dot{u} + u\nabla_\Gamma \cdot \mathbf{v} - a\Delta_\Gamma u = f(u,v) \qquad \text{in } (0,T) \times \Gamma \tag{1}$$

$$\dot{v} + v\nabla_\Gamma \cdot \mathbf{v} = g(u,v) \qquad \text{in } (0,T) \times \Gamma, \tag{2}$$

where

$$f(u,v) = \frac{1}{\epsilon} u \left(1 - u\right) \left(u - \frac{v+b}{c}\right)$$

$$g(u,v) = u - v,$$

with initial conditions

$$u(0,\cdot) = u_0(\cdot)$$

$$v(0,\cdot) = v_0(\cdot),$$

and model parameters a, b, c and ϵ all in $\mathbb{R}^+$.

The vector $\mathbf{v}$ is the surface velocity. It is zero when the surface is fixed. For a moving surface $(\Gamma_t)_{t \leq T}$,

$$\mathbf{v}(t, \Phi(t,x)) = \frac{\partial}{\partial t} \Phi(t,x),$$

where $\Phi : [0,T] \times \Gamma_0$ describes the deformation:

$$\Phi(t,\cdot) : \Gamma_0 \to \Gamma_t \text{ is a diffeomorphism,}$$

$$\Phi(0,\cdot) \text{ is the identity.}$$

We also define $\Phi_s^t : \Gamma_s \to \Gamma_t$ to be the transporting function:

$$\Phi_s^t = \Phi(t, \Phi(s,\cdot)^{-1}).$$

2

When the surfaces on which we implement this model have no boundary (like spheres), obviously boundary conditions are not required; when they do have a boundary (for example, spheres with holes), we use the Neumann boundary conditions

$$\nabla_\Gamma u(x) \cdot \mu(x) = 0 \qquad \forall x \in \partial\Gamma,$$

where μ is the outer unit conormal of Γ. This particular model is known as the *Barkley model*. Our justification for using the Barkley model is threefold: it has been shown to produce spiral waves, is relatively simple and is numerically efficient (see the conclusion of [5]).

Analysis of model   For convenience, let us define $u_{th} = \frac{v+b}{c}$. We focus on a phase portrait approach in understanding the dynamics of the Barkley model.

Ignoring the diffusion term for now, the nullclines (these are the (u, v) curves where $\dot{u}$ or $\dot{v}$ are zero) of the model are

$$u = \begin{cases} 0 \\ 1 \\ u_{th} \end{cases} \qquad \text{and} \qquad v = u. \tag{3}$$

Parts of these nullclines are sketched in Figure 3.
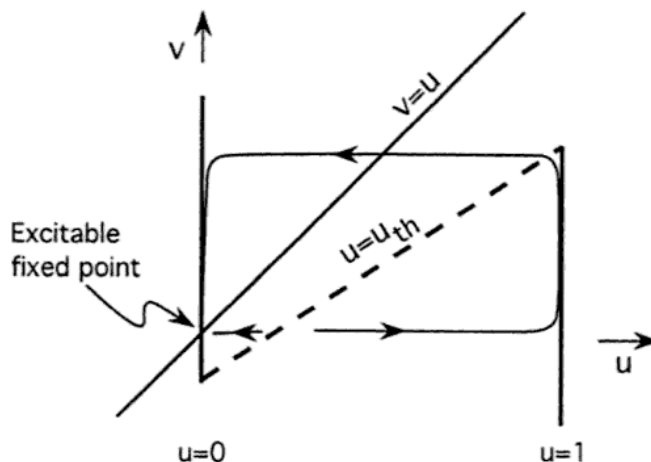
Figure 3: Partial phase portrait of the Barkley model (from [10, p. 167])

Clearly, (3) suggests that $u = v = 0$ is a fixed point of the system as both $\dot{u}$ and $\dot{v}$ are zero here. In fact, this fixed point is linearly stable [10, p. 167], meaning that all points close enough to the fixed point converge to it. Here by 'points', we mean initial conditions. So if the model is started with initial conditions close enough to $(u, v) = (0, 0)$, we end up in the state $u = v = 0$. What do we mean by 'close enough'? As the diagram suggests, if the initials conditions are such that u_0 exceeds u_{th}, then the system hits $u = 1$ before reaching the fixed point $u = v = 0$. If u_0 is below u_{th}, then we simply get decay of u to 0 directly. This u_{th} is what is called the *excitability threshold*, and we say that the fixed point at the origin is *excitable*.

It is clear that increasing $\frac{b}{c}$ (which has the effect of moving the $u = u_{th}$ line to the right) increases the excitation threshold. Reincorporating the diffusive term allows for waves of excitation to travel [10, p. 168].

Heuristically, increasing the parameter a increases the period of excitation and ϵ denotes the timescale separation between u and v.

3

Choice of parameters   We fix the model parameters to be

$$\epsilon = \frac{1}{50}, \quad b = \frac{1}{100}, \quad c = \frac{3}{4}$$

for all our simulations, leaving the remaining parameter a to be defined later. A justification for this is given in Section 2.4.

Types of surfaces   We consider three different kinds of surfaces Γ:

1. **Squares** One simple case we are interested in testing is the spiral evolution on a square, in which $\Gamma \subset \mathbb{R}^2$. Here, $\dot{u}$ and $\dot{v}$ are the usual time derivatives and $\Delta_\Gamma = \Delta$ is the Laplacian.

2. **2D Fixed Surface** The walls of heart chambers are a 2D surface that cannot be embedded in $\mathbb{R}^2$, unlike the square. So it is more realistic to model the equations on such surfaces like spheres and ellipsoids. In this case $\dot{u}$ and $\dot{v}$ are again the usual time derivatives however Δ_Γ is now the Laplace-Beltrami operator (The definition can be found in [8]).

3. **Moving Surfaces** The pulsation of the heart requires us to simulate the spiral waves on moving surfaces, where $\dot{u}$ and $\dot{v}$ are material derivatives (the definition can be found in [8]) and Δ_Γ is the Laplace-Beltrami operator on Γ_t; we suppress the subscript t when no ambiguity occurs.

1.3   Numerical Methods

The Barkley model has no known analytic general solution, so we seek a numerical solution. Let us detail the process of discretising in space and time. A more detailed description of the analysis behind the numerical scheme with extensive error analysis can be found in [8].

1.3.1   Finite Difference Method

Time Discretisation   Starting with the equations (1) and (2), discretise in time with the θ-scheme with timestep τ to give

$$T_\theta u^{n+1} = T_{\theta-1} u^n + \tau \tilde{f}^n; \tag{4}$$

$$v^{n+1} = v^n + \tau \tilde{g}^n, \tag{5}$$

where T_θ is the linear operator defined by

$$(T_\theta u)(x) = u(x) - \theta \tau a \Delta_\Gamma u(x),$$

$\tilde{f}^n = \tilde{f}^n(u^n, u^{n+1}, v^n, v^{n+1})$ is the term involving f and $\tilde{g}^n = \tilde{g}^n(u^n, u^{n+1}, v^n, v^{n+1})$ is the one involving g (which will be discussed later). We also need to discretise the space, which the following section addresses.

Space discretisation   We mainly focus on the excitation variable u because the equation for v is much more straightforward and will be discussed afterwards. When we are only simulating the equations on Ω_L, a square with side length L, FD is a simple and fast way to produce results. By dividing each coordinate axis into $N + 1$ evenly-spaced points which we denote by $(x_i)_0^N$ and $(y_i)_0^N$, the solution is approximated by interpolations from the vectors $(u^n(x_i, y_j))_{i,j=0}^N$. Let $h = l/N$. Both the Laplacian

$$\Delta u^n(x_i, y_j) \approx \Delta_h u^n(x_i, y_j)$$
$$= \frac{1}{h^2} \left(u^n(x_{i+1}, y_j) + u^n(x_{i-1}, y_j) - 4u^n(x_i, y_j) + u^n(x_{i-1}, y_j) + u^n(x_i, y_{j-1}) \right),$$

and the Neumann boundary condition

$$u^n(x_{-1}, y_j) = u^n(x_1, y_j), \quad u^n(x_{N+1}, y_j) = u^n(x_{N-1}, y_j),$$
$$u^n(x_i, y_{-1}) = u^n(x_i, y_1), \quad u^n(x_i, y_{N+1}) = u^n(x_i, y_{N-1}),$$

for $i, j = 0, ...N$, are approximated using the central difference.

Then T_θ is approximated by matrices $A_{\theta,h} = I - \theta\tau a\Delta_h$ operating on vectors u^n, hence if (and only if) $\tilde{f}^n$ is linear with respect to u^{n+1}, then (4) is reduced to a system of linear equations:

$$A_{\theta,h}u^{n+1} = A_{\theta-1,h}u^n + \tilde{f}^n. \tag{6}$$

1.3.2 Surface Finite Element Method

We then discretise in space using surface finite elment method (FE), about which a more detailed description of the analysis behind the numerical scheme with extensive error analysis can be found in [8]. This discretisation can be done on any type of surface. Multiplying by a test function $\phi\colon \mathcal{G}_T \to \mathbb{R}$ $\left(\text{where } \mathcal{G}_T = \bigcup_{t\in[0,T]}(\{t\} \times \Gamma_t)\right)$ such that $\phi(t, \cdot) \in H^1(\Gamma_t)$ and integrating, we obtain the weak formulation of equation (4):

$$\int_{\Gamma_t} \dot{u}\phi + \int_{\Gamma_t} u\phi\nabla_{\Gamma_t} \cdot \mathbf{v} + \int_{\Gamma_t} a\nabla_{\Gamma_t}u \cdot \nabla_{\Gamma_t}\phi = \int_{\Gamma_t} f(u,v)\phi.$$

By using the Leibniz formula, this becomes

$$\frac{d}{dt}\int u\phi + \int a\nabla_\Gamma u \cdot \nabla_\Gamma\phi = \int f(u,v)\phi + \int u\dot{\phi}.$$

The work in [8] shows that by considering a set of m-dimensional spaces $V_t \subset H^1(\Gamma_t)$, a set of basis functions $(Z_i(t, \cdot))_{i\leq m}$ can be chosen such that $\dot{Z}_i = 0$ for all i. Therefore plugging $\phi = Z_i$ into the previous equation, we have

$$\frac{d}{dt}\int uZ_i + \int a\nabla_\Gamma u \cdot \nabla_\Gamma Z_i = \int f(u,v)Z_i.$$

Therefore discretising in time and applying θ method, we have

$$\int_{\Gamma_{(n+1)\tau}} u^{n+1}Z_i^{n+1} + \theta a\nabla_\Gamma u^{n+1} \cdot \nabla_\Gamma Z_i^{n+1} = \int_{\Gamma_{n\tau}} u^n Z_i^n + (\theta - 1)a\nabla_\Gamma u^n \cdot \nabla_\Gamma Z_i^n + \tilde{F}^n,$$

where $u^n = u(n\tau, \cdot)$, $Z^n = Z(n\tau, \cdot)$ and $\tilde{F}^n$ is the integral containing f. This yields

$$a_\theta^{n+1}(u^{n+1}, Z_i^{n+1}) = a_{\theta-1}^n(u^n, Z_i^n) + \tilde{F}^n, \tag{7}$$

where $a_\theta^n\colon H^1(\Gamma_{n\tau}) \times H^1(\Gamma_{n\tau}) \to \mathbb{R}$ is a bilinear form defined by

$$a_\theta^n(\xi, \eta) = \int_{\Gamma_{n\tau}} (\xi\eta + \theta a\nabla_\Gamma\xi \cdot \nabla_\Gamma\eta).$$

FEM aims at approximating u^n by its projection on V. This allows us to write u^n as

$$u^n \approx P_V(u^n) = \sum_{i=1}^N \alpha_i^n Z_i^n$$

5

with coefficients $\alpha_i^n \in \mathbb{R}$, which are to be solved for. For simplicity we identify u^n with $P_V(u^n)$. Then the equation (7) can be rewritten as:

$$\sum_{j=1}^m \alpha_j^{n+1} a_\theta^{n+1}(Z_j^{n+1}, Z_i^{n+1}) = \sum_{j=1}^m \alpha_j^n a_{\theta-1}^n(Z_j^n, Z_i^n) + \tilde{F}^n$$

for $i = 1, ..., m$. Hence if $\tilde{F}^n$ is linear with respect to α_j^{n+1}, $j \leq m$, then (4) is again reduced to a system of linear equations.

1.3.3 Approximating the right hand side

Now let us discuss how to deal with $\tilde{f}^n$ and $\tilde{F}^n$ terms in the time and space discretization. If we work strictly in line with θ-method, then the respectively $\tilde{f}^n$ in (4) and $\tilde{F}^n$ in (7) are

$$\tilde{f}^n = \tau\theta f(u^{n+1}, v^{n+1}) + \tau(1-\theta)f(u^n, v^n). \tag{8}$$

$$\tilde{F}^n = \tau\theta \int_{\Gamma_{(n+1)\tau}} f(u^{n+1}, v^{n+1})Z_i^{n+1} + \tau(1-\theta) \int_{\Gamma_{n\tau}} f(u^n, v^n)Z_i^n$$

$$= \tau\theta \int_{\Gamma_{(n+1)\tau}} f\left(\sum_j \alpha_j Z_j^{n+1}, v^{n+1}\right) Z_i^{n+1} + \tau(1-\theta) \int_{\Gamma_{n\tau}} f(u^n, v^n)Z_i^n.$$

When $\theta > 0$, f is nonlinear with respect to u^{n+1}, which would inflict intolerable pains if one tries to implement (as we no longer have a simple matrix equation), especially when we set $\theta = 1$ for sake of stability. We consider two ways of solving this problem.

Explicit method One solution is to consider $\tilde{f}^n$ and $\tilde{F}^n$ fully explicitly regardless of θ in time discretisation:

$$\tilde{f}^n = f(u^n, v^n)$$

$$\tilde{F}^n = \tau \int_{\Gamma_{n\tau}} f(u^n, v^n)Z_i^n.$$

Then the the FD method (6) becomes a system of linear equations:

$$A_{\theta,h} u^{n+1} = A_{\theta-1,h} u^n + f(u^n, v^n).$$

And the FE method (7):

$$\sum_{j=1}^m \alpha_j^{n+1} a_\theta^{n+1}(Z_j^{n+1}, Z_i^{n+1}) = \sum_{j=1}^m \alpha_j^n a_{\theta-1}^n(Z_j^n, Z_i^n) + \int f(u^n, v^n)Z_i^n; \quad \forall i = 1, \dots, m.$$

We call this *explict RHS method*. It requires a small time step to ensure stability.

Semi-implicit method An alternative method to the explicit method is to test with a *semi-implicit* RHS, which is half-way between fully explicit (as described in the previous solution) and fully implicit (which is what we would obtain in the $\theta-$scheme with $\theta = 1$). It has the advantage of allowing for a larger timestep without succumbing to numerical instability unlike the explicit RHS. The idea is as follows. First, consider the FD method. Since our f is a factorized cubic polynomial, take

$$\tilde{f}^n = \frac{1}{\epsilon} u^{n_1}(1 - u^{n_2})\left(u^{n_3} - \frac{v^{n_3} + b}{c}\right),$$

where n_1, n_2, n_3 are either n or $n + 1$. When $n_1 = n_2 = n_3 = n$, $\tilde{f}^n$ is the fully explicit RHS described in previous section. When $n_1 = n_2 = n_3 = n + 1$, $\tilde{f}^n$ is the fully implicit RHS, i.e., take $\theta = 1$ in (8). The semi-implicit method takes two of the n_i to be n and the remaining one to be $n + 1$ to make $\tilde{f}^n$ linear in u^{n+1}. Exactly which n_i is to be taken as $n + 1$ depends on the excitability threshold

$$u_{th}^n = \frac{v^n + b}{c}.$$

When $u_{th}^n < u^n$, take $n_1 = n + 1$; when $u_{th}^n \geq u^n$, we take $n_2 = n + 1$. Then (6) becomes:

$$\left(A_{\theta,h} + \frac{\tau}{\epsilon} u^n (u^n - u_{th}^n) I \right) u^{n+1} = A_{\theta-1,h} u^n + \frac{\tau}{\epsilon} u^n (u^n - u_{th}^n) \quad \text{when } u_{th}^n < u^n,$$

$$\left(A_{\theta,h} - \frac{\tau}{\epsilon} (1 - u^n)(u^n - u_{th}^n) I \right) u^{n+1} = A_{\theta-1,h} u^n + \tilde{f}^n \qquad \text{when } u_{th}^n \geq u^n,$$

where I is the identity matrix.

For the FE method a corresponding semi-implicit $\tilde{F}^n$ is

$$\tilde{F}^n = \begin{cases} \frac{\tau}{\epsilon} \int_{\Gamma_{(n+1)\tau}} u^{n+1} (1 - \bar{u}^n)(\bar{u}^n - \bar{u}_{th}^n), & \text{if } u_{th}^n < u^n; \\ \frac{\tau}{\epsilon} \int_{\Gamma_{n\tau}} u^n (u^n - u_{th}^n) - \frac{\tau}{\epsilon} \int_{\Gamma_{(n+1)\tau}} \bar{u}^n (\bar{u}^n - \bar{u}_{th}^n) u^{n+1}, & \text{if } u_{th}^n \geq u^n, \end{cases}$$

where the $\bar{u}^n = u^n \circ \Phi_{(n+1)\tau}^{n\tau}$ and $\bar{u}_{th}^n = u_{th}^n \circ \Phi_{(n+1)\tau}^{n\tau}$ are u^n and u_{th}^n taking values at mapped points. Then (7) becomes a system of linear equations:

$$\sum_{j=1}^{m} \alpha_j^{n+1} \left(a_\theta^{n+1}(Z_j^{n+1}, Z_i^{n+1}) - \frac{\tau}{\epsilon} \int Z_j^{n+1}(1 - \bar{u}^n)(\bar{u}^n - \bar{u}_{th}^n) \right) = \sum_{j=1}^{m} \alpha_j^n a_{\theta-1}^n(Z_j^n, Z_i^n)$$

$$\text{when } u_{th}^n < u^n, \text{ and}$$

$$\sum_{j=1}^{m} \alpha_j^{n+1} \left(a_\theta^{n+1}(Z_j^{n+1}, Z_i^{n+1}) - \frac{\tau}{\epsilon} \int Z_j^{n+1} \bar{u}^n (\bar{u}^n - \bar{u}_{th}^n) \right) = \sum_{j=1}^{m} \alpha_j^n a_{\theta-1}^n(Z_j^n, Z_i^n)$$

$$+ \frac{\tau}{\epsilon} \int u^n (u^n - u_{th}^n)$$

$$\text{when } u_{th}^n \geq u^n$$

for all $i = 1, \ldots, m$.

1.3.4 The recovery variable v

Solving v is a much simpler task than u due to its ODE-like equation.

When using FD for space discretisation, g^n is treated fully explicitly:

$$\tilde{g}^n(u^n, v^n, u^{n+1}, v^{n+1}) = g(u^n, v^n).$$

Hence the scheme for v is explicit:

$$v^{n+1} = v^n + \tau g(u^n, v^n).$$

When using the FE method, we also treat g explicitly and we treat v in the same way as u, i.e.,

$$\sum_{j=1}^{m} \beta_j^{n+1} \int Z_j^{n+1} Z_i^{n+1} = \sum_{j=1}^{m} \beta_j^n \int Z_j^n Z_i^n + \tau \int g(u^n, v^n) Z_i^n, \quad \forall i = 1, \ldots, m,$$

where β_j^n's are the coordinates of v^n in $V_{n\tau}$:

$$v^n = \sum_{j=1}^{m} \beta_j^n Z_j^n.$$

For the finite element simulations that we will develop in the later sections, we make use of the Distributed and Unified Numerics Environment (DUNE) software [14]. Material on the finite element method can be found at [3], and for information about the iterative solvers used, see [7]. The theory of the DUNE grid is described in [13].

2 Proposed Experiments

In this section, we detail the various experiments that we wish to conduct in our simulations.

2.1 Fixed Sphere

We start with the simplest case where we fix the surface Γ to be a (static) unit sphere. This is obviously not a very realistic model of the heart as it does not account for the movement of the heart and the heart is not spherical. Therefore we begin by developing a simulation on a more realistic ellipsoid. We form the ellipsoid by extending the sphere along the y-axis.

2.2 Moving Surfaces

As stated above, the heart pulsates and so has spatial movement which we wish to incorporate. We would also like to deform the surface to one that more closely resembles the human heart. We initially add a sinusoidal deformation onto one of the coordinates so that we have a pulsating ellipsoid.

2.3 Inhomogeneities

For various reasons, heart tissue can become damaged. This leads to different electro-dynamical properties. The damaged tissue may not conduct electricity as well as the healthy tissue and so the action potential cannot travel across these regions unimpeded. This leads to *inhomogeneities* or *holes* in the domain, which we can implement in a number of ways.

In what follows, when we say the diffusive flux or conductivity we mean the coefficient in front of the Laplacian term in (1).

2.3.1 No conductivity

To model the scenario in which the damaged tissue does not conduct *any* electricity at all, we can set the diffusive flux (which models the conductivity) to zero in a region (following [16, p. 2]). We expect that the finite element method may have some problems in implementing this as there is a sudden discontinuous jump in the diffusivity constant in the region of the hole. To get around this, we also consider the possibility of reducing the conductivity in the area of interest by a multiplicative factor instead of killing it completely.

2.3.2 Reduced conductivity

As alluded to above, we reduce the diffusive flux by a factor of 100 in regions where the tissue is damaged. This can still lead to jumps but these are not as steep as in the previous case.

2.3.3 Continuous conductivity

As mentioned above, we expect that the numerical instabilities arising when regions of zero conductivity are created (by setting the diffusion constant to zero) are due to the sudden jump in the value of conductivity. Here we suggest another remedy for this: multiply the diffusive flux by a function which ensures that the conductivity decreases to zero at the centre of the hole in a continuous fashion. If we consider the hole to be circular then we can use a Gaussian function. In the region of the hole centred at $\mathbf{x}_0 = (x_0, y_0)$ we could multiply the diffusion coefficient by

$$1 - \exp\left(\frac{-|\mathbf{x} - \mathbf{x}_0|^2}{2\sigma_1^2}\right),$$

which is zero at the centre of the hole and has variance σ_1^2.

However if our hole has radius R then this coefficient will not be continuous on the boundary since there will still remain a residue of the Gaussian. We can solve this trivially by adding in the remainder of the Gaussian to give the multiplicative factor as

$$1 + \exp\left(\frac{-R^2}{2\sigma_1^2}\right) - \exp\left(\frac{-|\mathbf{x} - \mathbf{x}_0|^2}{2\sigma_1^2}\right),$$

so that on the boundary of the hole, this factor is exactly 1. But this is no longer zero at the center of the hole. Therefore we supplement this with another exponential factor so that the factor decays quickly to zero at the centre:

$$1 + \exp\left(\frac{-R^2}{2\sigma_1^2}\right) \times \exp\left(\frac{|\mathbf{x} - \mathbf{x}_0|^2 - R^2}{2\sigma_2^2}\right) - \exp\left(\frac{-|\mathbf{x} - \mathbf{x}_0|^2}{2\sigma_1^2}\right)$$

where $\sigma_2^2 \ll \sigma_1^2$. The values of these variances must be carefully chosen. A small variance σ_1^2 gives holes where the coefficients agree on the edges but the sides of the hole are very steep, and for most of the hole the diffusion coefficient is close to its unadulterated value. If, on the other hand, we have a large σ_1^2, the contribution of the second Gaussian is greater and we are further from the true Gaussian (as the remainder term from the first Gaussian is larger). Using the standard belief that five standard deviations of the mean is statistically significant we take $\sigma_1^2 = 5R$ and we choose σ_2^2 such that $\frac{1}{2\sigma_2^2} = 1000$.

With these choices we have

$$1 + \exp\left(\frac{-R}{10}\right) \times \exp\left(1000\left(|\mathbf{x} - \mathbf{x}_0|^2 - R^2\right)\right) - \exp\left(\frac{-|\mathbf{x} - \mathbf{x}_0|^2}{10R}\right)$$

as the multiplicative factor of the diffusive flux.

2.3.4 Surfaces with holes

The heart is punctured by various blood vessels like veins and arteries. The correct way to simulate this is to filter out various elements used to construct the sphere and apply zero Neumann boundary conditions on the new boundary. This method is also suitable for approximating areas of heart tissue where the wave can no longer propagate.

2.4 An Excursion on Parameter Choice and Numerical Stability

Before moving on, it is necessary to explain the choice of parameters we use to simulate the Barkley equation. Define Ω_c for $c \in \mathbb{R}^+$ to be the interval $[0, c]^2$. From a former experiment we

know that by setting

$$\Gamma = \Omega_{150}, \quad \epsilon = \frac{1}{50}, \quad a = 1, \quad b = \frac{1}{100}, \quad c = \frac{3}{4},$$

$$u_0 = \mathbb{I}_{\frac{y}{150} > \frac{51}{100}}, \quad v_0 = \frac{3}{8}\mathbb{I}_{\frac{x}{150} < \frac{1}{2}} \tag{9}$$

a spiral $u\colon \Omega_{150} \to [0,1]$ can be successfully produced using FD with the semi-implicit method. Because we want to test the model on a unit sphere, some rescaling is necessary. Suppose we want to simulate a spiral with similar relative scale on Ω_L, i.e., we want to solve $\tilde{u}, \tilde{v} : \Omega_L \to [0,1]$ satisfying

$$\tilde{u}(t,x) = u\left(t, \frac{150}{L}x\right) \qquad \text{and} \qquad \tilde{v}(t,x) = v\left(t, \frac{150}{L}x\right).$$

Plugging u into the equations (1) and (2) with the previous parameters we can obtain the Barkley equation for $\tilde{u}$:

$$\tilde{u}_t - \frac{L^2}{150^2}\Delta\tilde{u} = f(\tilde{u}, \tilde{v}),$$

$$\tilde{v}_t = g(\tilde{u}, \tilde{v}),$$

with the same parameters (9) except for Γ and a. Because we want to test on a unit sphere and also on a square with the same area, we set

$$L = 3.5 \approx 2\sqrt{\pi},$$

and

$$a = \frac{1}{1790.49} \approx \frac{4\pi}{150^2}.$$
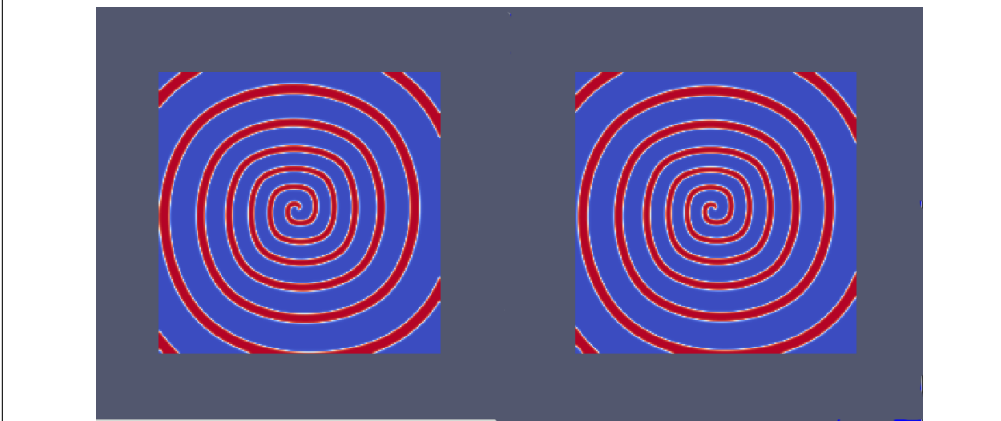
For the effect, see Figure 4.

Figure 4: The solution with different scales, at time 25, using FD semi-implicit method.
Left: $\Gamma = \Omega_{3.5}$, $a = \frac{1}{1790.49}$. *Right*: $\Gamma = \Omega_{150}$, $a = 1$.
The two figures are scaled to the same size and the spirals are almost the same.

Usually we have two criteria in deciding whether a simulation is stable. The first is, regarding the FD semi-implicit code as reliable, comparing the results of all other codes to those of the FD semi-implicit code. The second is to observe whether the maximum principle holds. If the approximate solution u of a simulation noticeably exceeds $[0,1]$, we suppose that the simulation

fails. Based on these standards we find that the FEM does not give stable results for such small values of a. Therefore we reset

$$a = \frac{1}{179.049}$$

and obtain thicker spirals. We tested various possibilities in between; for example,

$$a = \frac{2}{1790.49}, \frac{1}{500}, \frac{1}{350}, \frac{1}{250},$$

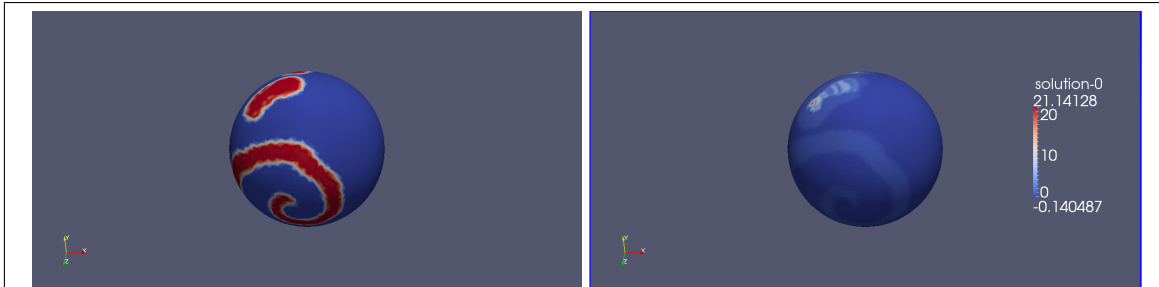all of which gave unstable results. See Figure 5 through to Figure 7.

Figure 5: Using FEM semi-implicit method on a unit sphere with $a = \frac{2}{1790.49}$.
Left: at time 6.5, the red part at the top is supposed to disappear but instead starts growing.
Right: at time 7.1, the maximum of u has grown far more than 1, which implies instability.
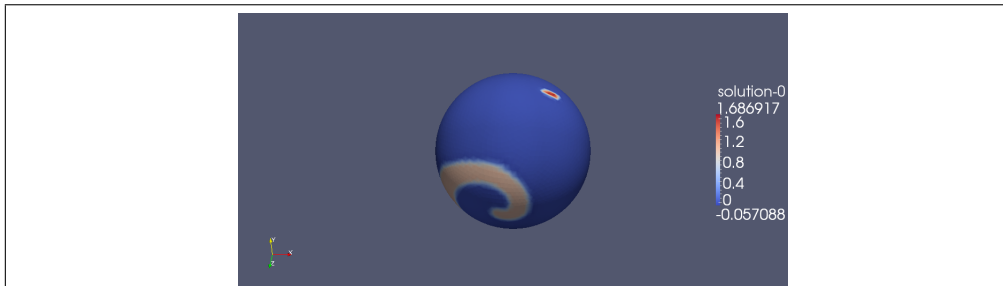
Figure 6: With $a = \frac{1}{250}$, result is better than the case $a = \frac{2}{1790.49}$: the spiral is more regular and the top red part is vanishing as expected, however the overshoot is still unacceptable.

We will be concerned with numerical stability frequently in the following sections.

Figure 7: Tests on $\Omega_{3.5}$ with $a = \frac{1}{1790.49}$ at time 10.
Top left: using FD explicit method. *Top right*: using FEM explicit method.
Bottom left: using FD semi-implicit method. *Bottom right*: using FEM semi-implicit method.
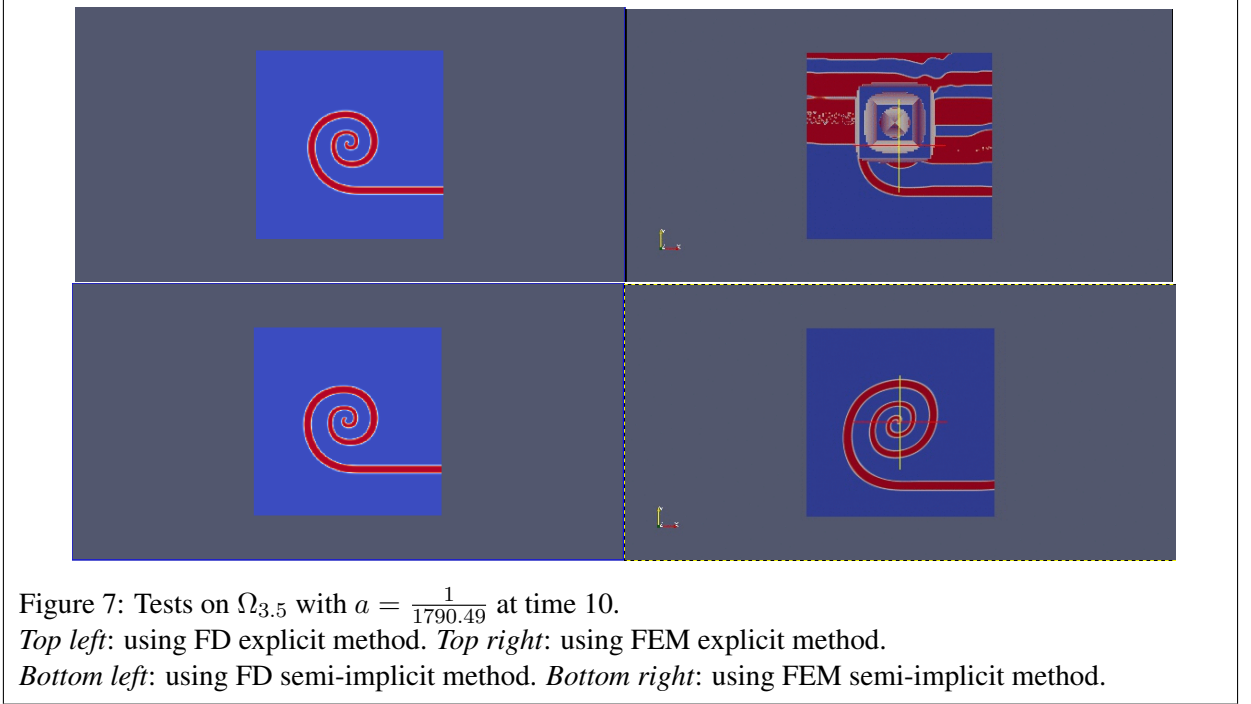
3 Planar 2D Simulation

As we mentioned in Section 2.4, to ensure that the FEM implementation for fixed surfaces, moving surfaces and inhomogeneous surfaces are correct, we start with tests on the square $\Omega_{3.5}$ and compare it with the FD implementation.
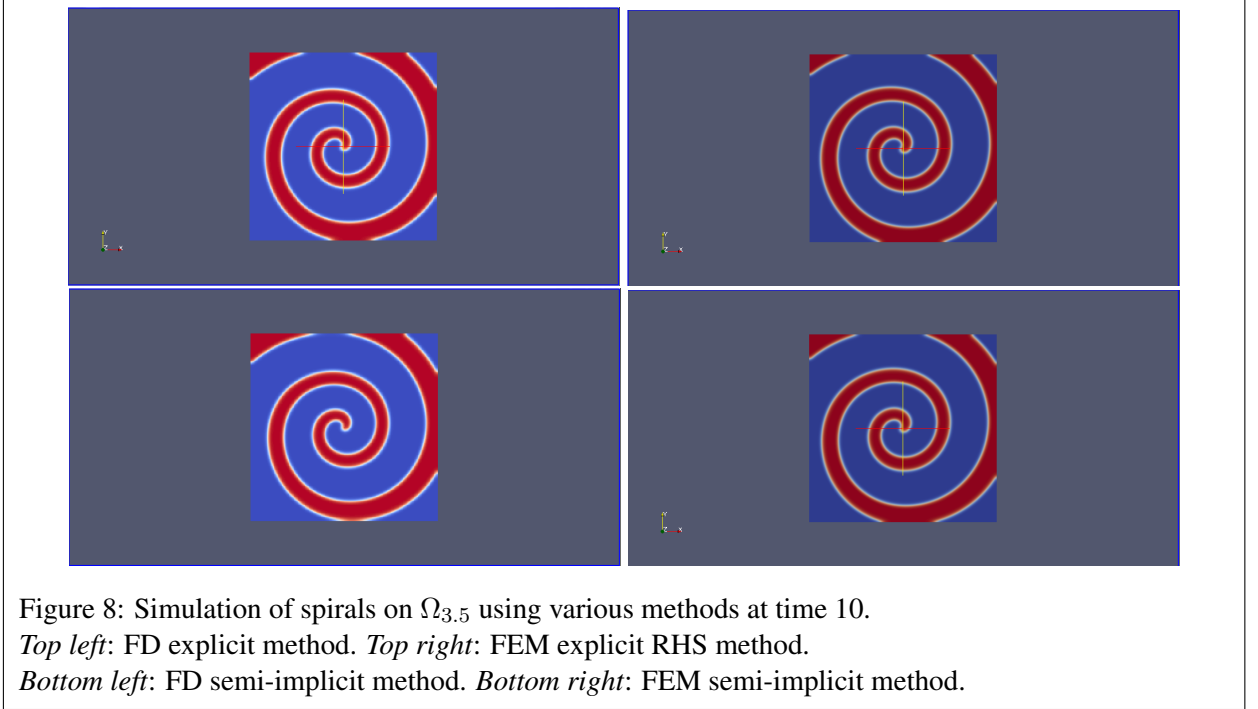
3.1 Results

Taking

$$\Gamma = \Omega_{3.5}, \quad \epsilon = \frac{1}{50}, \quad a = \frac{1}{179.049}, \quad b = \frac{1}{100}, \quad c = \frac{3}{4},$$

we compare the results by FD and FEM. In FEM we take the initial conditions:

$$u_0(x,y) = \mathbb{I}_{y>1.751};$$
$$v_0(x,y) = \mathbb{I}_{x<1.75}.$$

Figure 8 contains the results of different methods. One can see that they are almost identical.

Figure 8: Simulation of spirals on $\Omega_{3.5}$ using various methods at time 10.
Top left: FD explicit method. *Top right*: FEM explicit RHS method.
Bottom left: FD semi-implicit method. *Bottom right*: FEM semi-implicit method.

4 Fixed Spherical Surface Simulation

Instead of using Heaviside functions (denoting the spatial variable $\mathbf{x} = (x, y, z)$)

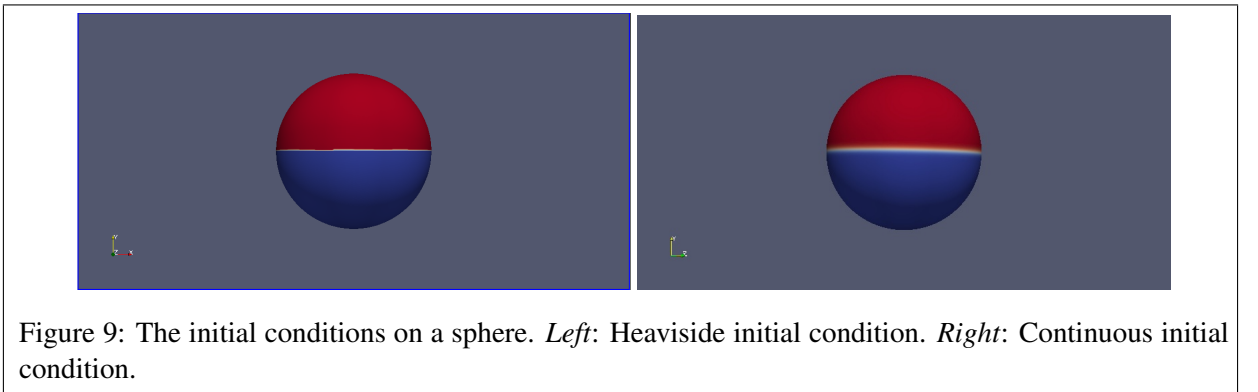$$u(0, \mathbf{x}) = u_0(\mathbf{x}) = \mathbb{I}_{y>0.01}$$
$$v(0, \mathbf{x}) = v_0(\mathbf{x}) = \frac{3}{8}\mathbb{I}_{x<0},$$

we use its continuous version

$$u(0, \mathbf{x}) = u_0(\mathbf{x}) = \frac{1}{2}(\tanh(30y) + 1)$$
$$v(0, \mathbf{x}) = v_0(\mathbf{x}) = \frac{1}{2}0.375(\tanh(30(-x + 0.01)) + 1)$$

as our initial conditions. For a visualisation of these conditions, see Figure 9.

Figure 9: The initial conditions on a sphere. *Left*: Heaviside initial condition. *Right*: Continuous initial condition.

We use the semi-implicit method in all of these simulations.

4.1 Fixed Spherical Surfaces

Grid refinement   Before working on further experiments, we refine the grid until the difference in the solutions between two consecutive refinements is negligible. Then we pick the less well-refined of the two refinements (since it is more efficient to compute and is almost as good as the better refinement). This ensures that we are looking at sensible results, i.e., that the results are solutions that are convergent, and not just a by-product of instability or happenstance, for example.
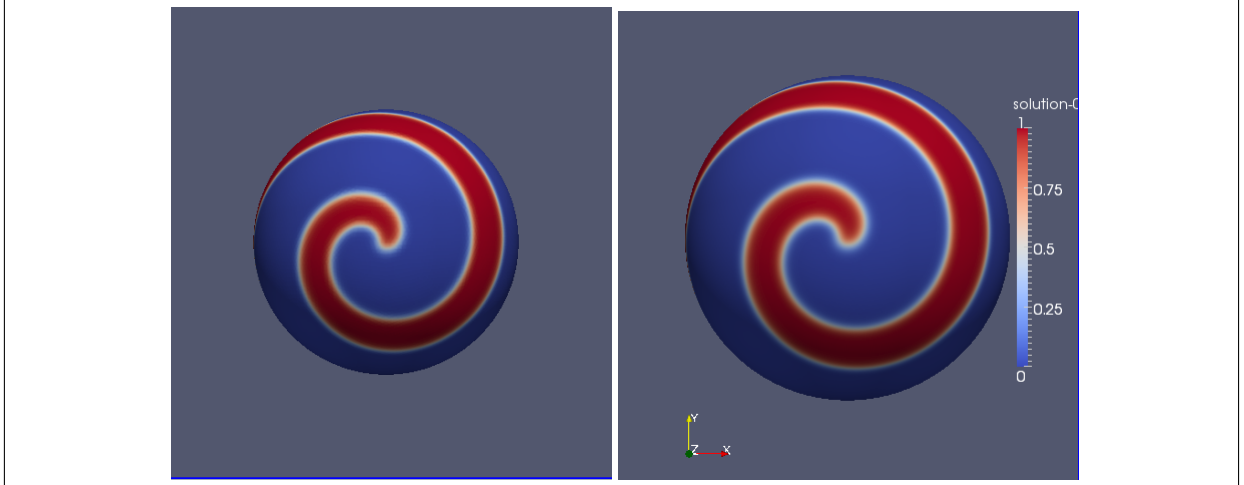
Figure 10: Change of resol. makes no diff.

Analysis   Using the semi-implicit method (the explicit method also gives similar results) with diffusion coefficient $a = \frac{1}{179.049}$ on the unit sphere, we obtain the following results in Figure 11. A spiral (call it the front spiral) can be seen to develop at time 6.7. Actually two spirals exist; the other one (call it the back spiral) is on the opposite side of the view in the figures. It can be seen from the last three figures that the location of the front spiral is slowly and steadily moving.

Because we will simulate spirals on the deforming ellipsoid (described later in Section 5), we are also interested in observing the spirals on a fixed ellipsoid. Using the same method, we test the Barkley model on an ellipsoid which has been deformed from a unit sphere by extension by a factor 1.5 along the y-axis. The results are displayed in Figure 12. This time we display it in an angle which allows the back spiral to be partly seen in the last two figures, symmetrically joining the front spiral. Although due to the difference in angle this cannot be compared directly with Figure 11, there is no qualitative difference in the evolution of the spirals between this ellipsoid and the sphere.
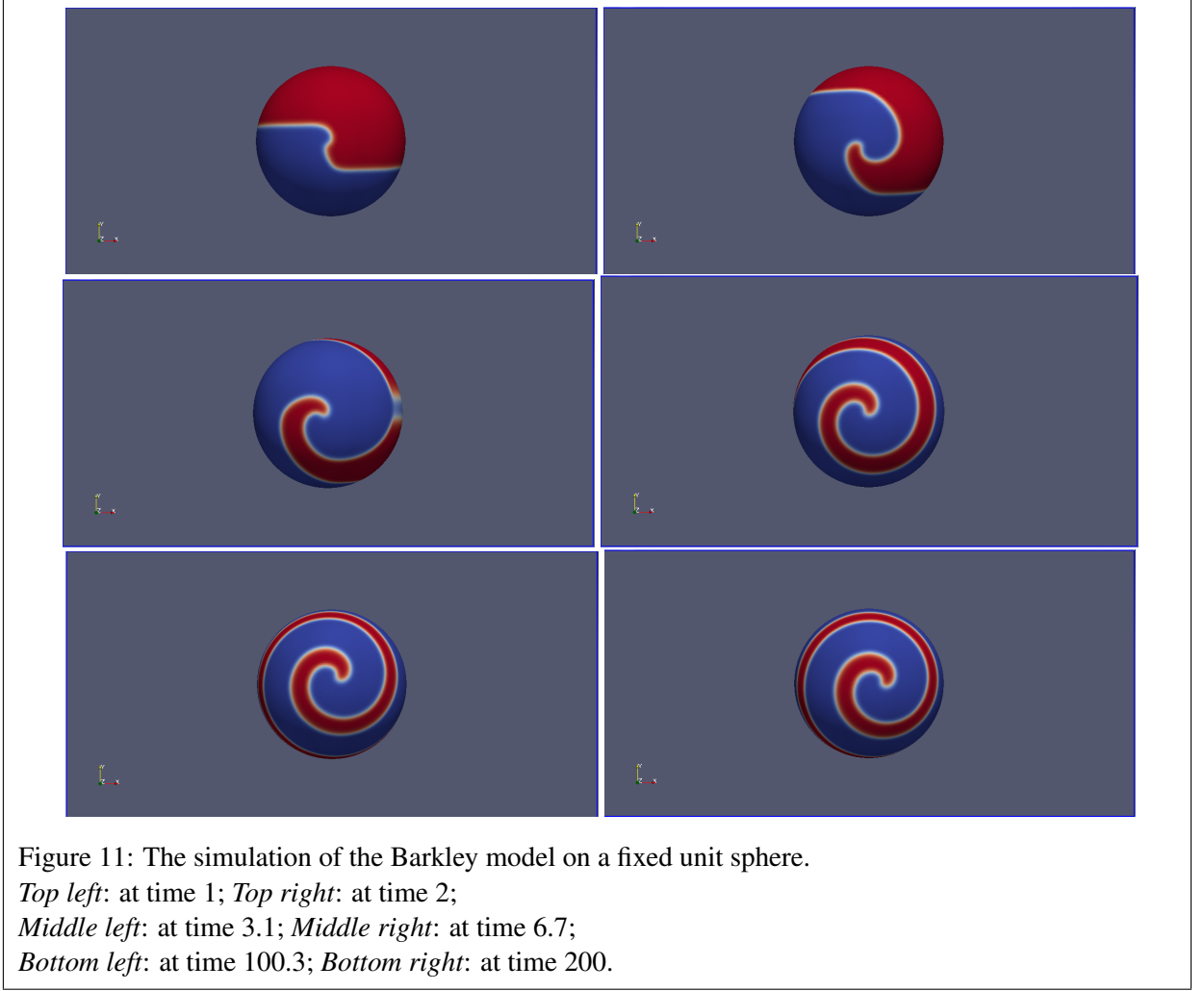
4.2 Fixed Sphere with Inhomogeneities

We simulate the effects of the inhomogeneities as described in Section 2.3 on a fixed sphere.

4.2.1 No conductivity

The results of setting the diffusive flux to zero in the region

$$\{(x, y, z) : 0.3 < x < 0.4, 0.3 < y < 0.4, z \geq 0\}$$

are shown below in Figure 13.

Figure 11: The simulation of the Barkley model on a fixed unit sphere.
Top left: at time 1; *Top right*: at time 2;
Middle left: at time 3.1; *Middle right*: at time 6.7;
Bottom left: at time 100.3; *Bottom right*: at time 200.

Analysis One can see that there are artefacts of the hole remaining after the spiral wave has passed the hole (see Figure 14).

The same figure shows that there is an overshoot (u is unreasonably bigger than 1 on these artefacts; recall that the solution should lie in the interval $[0, 1]$) in the solution on this artefact: this is as a result of numerical instability. So, like we anticipated, it seems that the method cannot properly handle a discontinuity in the diffusive flux.

4.2.2 Reduced conductivity

We want to test the Barkley model with the diffusive coefficient significantly smaller in certain regions (say Γ_I) than the rest of the unit sphere, i.e.,

$$a(\mathbf{x}) = \begin{cases} \frac{1}{17904.9}, & \mathbf{x} \in \Gamma_I \\ \frac{1}{179.049}, & \text{otherwise.} \end{cases}$$

We test two cases in which the inhomogeneities Γ_I are defined by:

$$\text{Test case 1: } \Gamma_I = \Gamma \cap \{(x - 0.15)^2 + y^2 < 0.01\} \cap \{z > 0\}, \tag{10}$$

$$\text{Test case 2: } \Gamma_I = \Gamma \cap \{(x - 0.35)^2 + y^2 < 0.09\} \cap \{z > 0\}. \tag{11}$$

We put the inhomogeneities close to the centre of the front spiral that develops in the fixed sphere case (see Figure 11) because we want to see the effect on the location of the spirals.

Figure 12: The simulation of spirals on a fixed unit ellipsoid $x^2 + \frac{4}{9}y^2 + z^2 = 1$.
Top left: at time 0; *Top right*: at time 1;
Middle left: at time 3; *Middle right*: at time 5;
Bottom left: at time 6.1; *Bottom right*: at time 7.4.
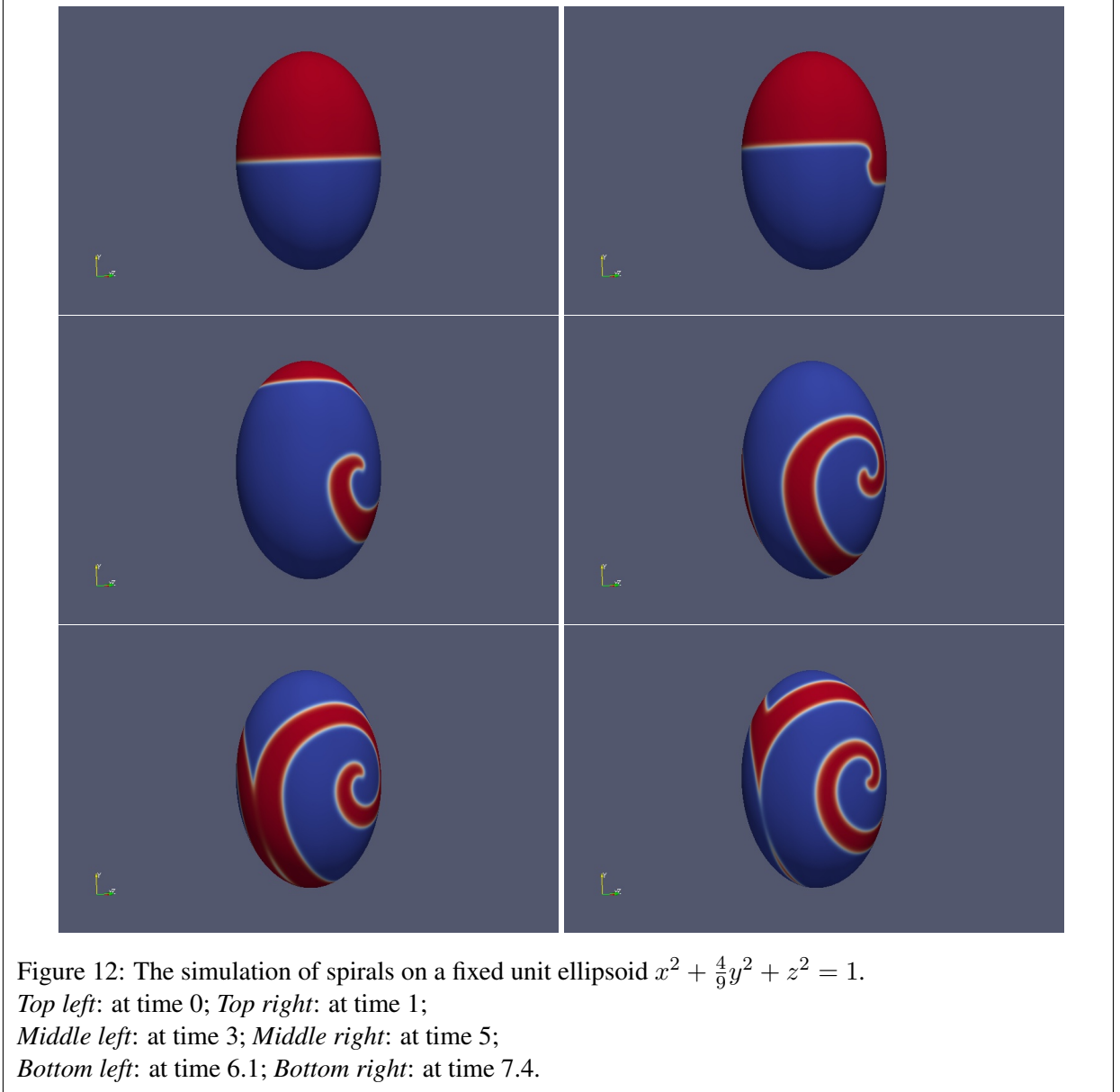
Analysis   The results of the first test are displayed in Figure 15. One can see that the evolution at locations away from the inhomogeneity is not affected, especially the middle left picture, which resembles the middle left picture of Figure 11. One can also find an overshoot of 1.167 in the top right picture of Figure 15. From the last three images, a downward movement of the centre of spiral can be noticed. Comparing it to the one in the fixed sphere implementation, we find that the hole affects the location of the centre of the spiral.

After testing the second case, we obtain some different animations. However, like the failure in the case of no conductivity in Section 4.2.1, the overshoot at time 3.4 implies instability (see Figure 16).

4.2.3   Continuous conductivity

For the case where the conductivity is smoothly reduced to zero, we consider two circular holes:

- Hole A; centred at $(0.3, 0.3, \sqrt{0.82})$ with radius 0.1, and

16
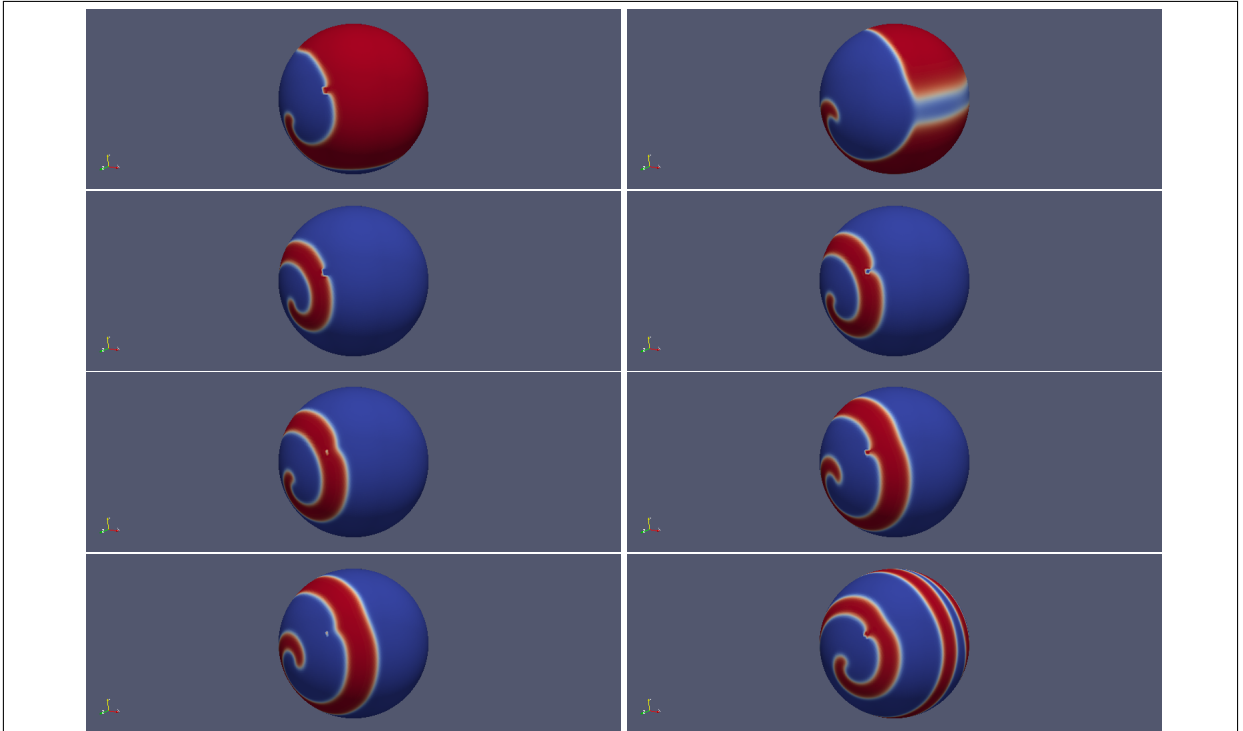
Figure 13: Sphere with region of zero conductivity.
Top left: at time 2.3; *Top right*: at time 3.1
Second row left: at time 5.1; *Second row right*: at time 5.5
Third row left: at time 5.7; *Third row right*: at time 6.5
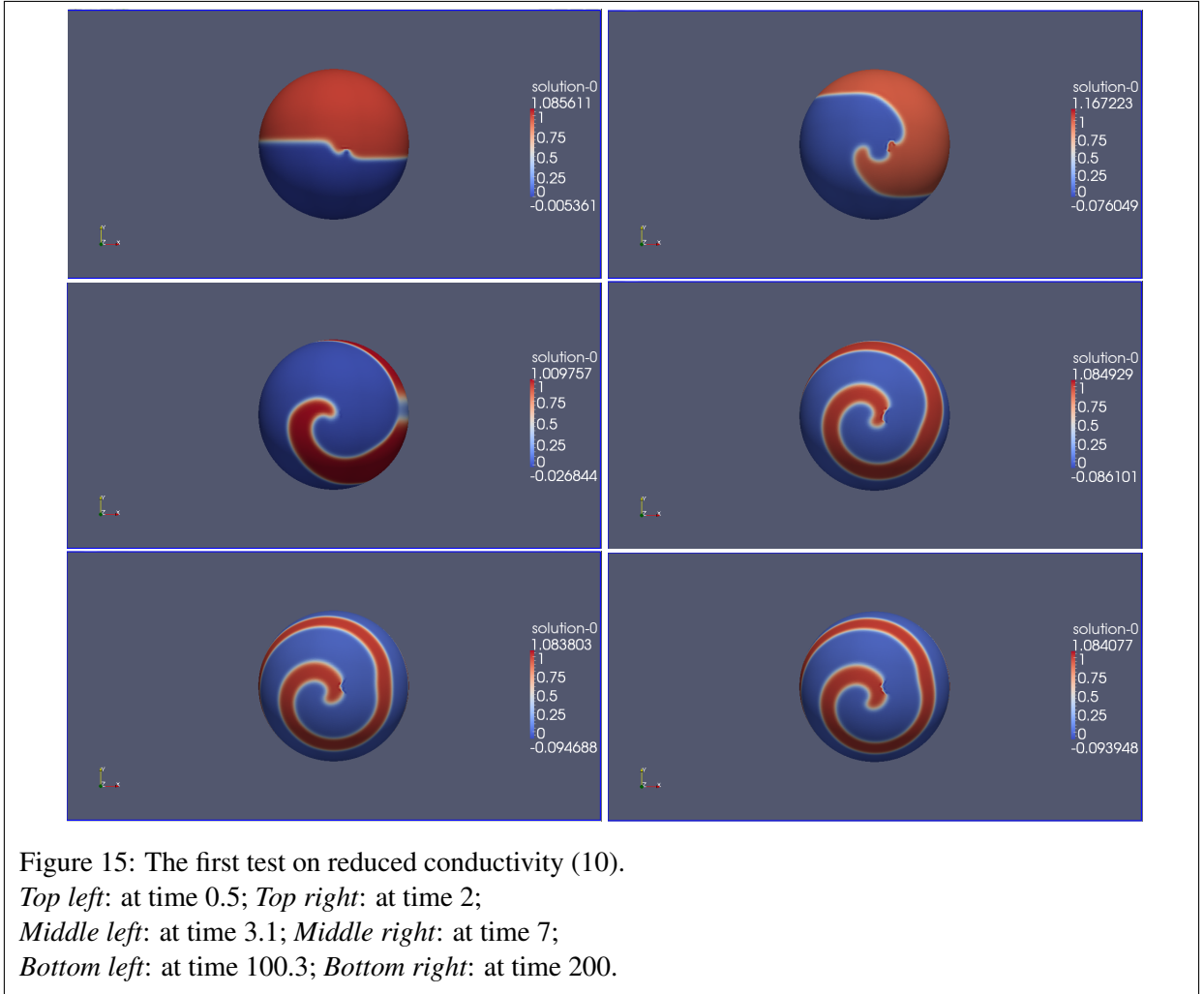*Bottom row left*: at time 6.8; *Bottom row right*: at time 20
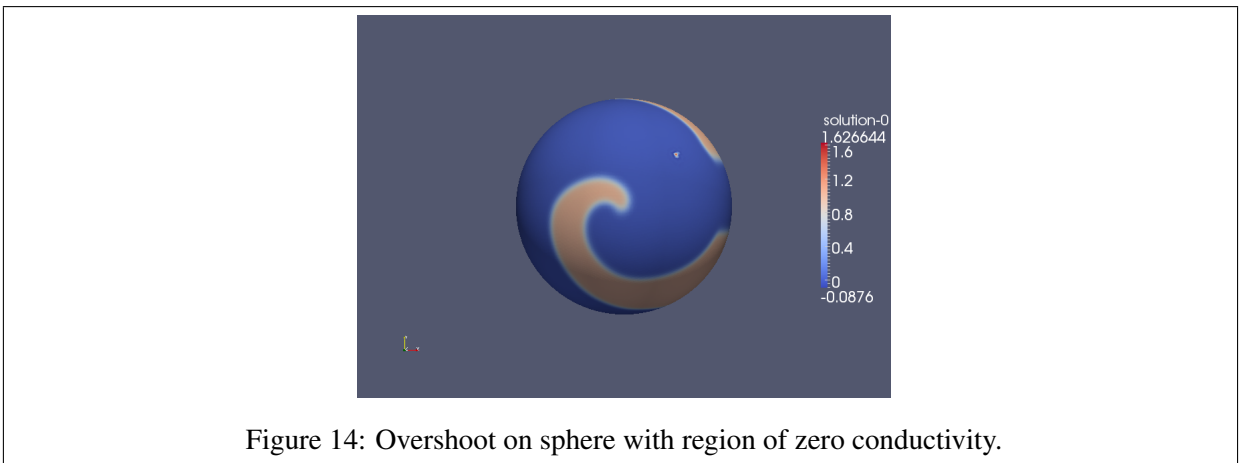
Figure 14: Overshoot on sphere with region of zero conductivity.

- Hole B; centred at $(0.3, -0.3, \sqrt{0.82})$ with radius 0.2.

See Figures 17, 18 and 19 for the results. Each image contains two simulations; the sphere with hole A is shown on the left and the sphere with hole B is on the right.

Analysis One can see that, in both cases, as the wave travels, the part of the wave that hits the hole slows down, with some regions of the hole appearing impenetrable at first (for example, see the bottom right image of Figure 17). One can also see artefacts (or excitation) left behind inside

Figure 15: The first test on reduced conductivity (10).
Top left: at time 0.5; *Top right*: at time 2;
Middle left: at time 3.1; *Middle right*: at time 7;
Bottom left: at time 100.3; *Bottom right*: at time 200.

Figure 16: The second test on reduced conductivity (11) at time 3.4.
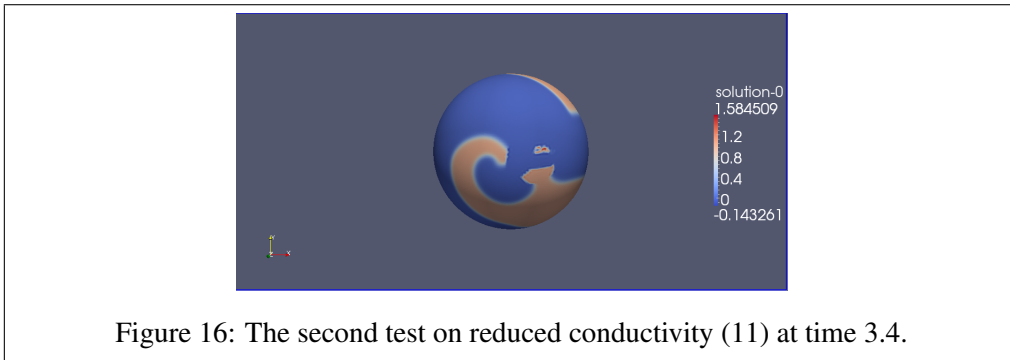
the hole long after the passage of the wave, as in the case of the top left image in Figure 18.

4.2.4 Surface with holes

In this, we remove a part of the sphere so as to model a physical hole. More precisely, we study two circular holes:

- Hole A; centred at $(0.3, 0.3, \sqrt{0.82})$ with radius 0.1, and

- Hole B; centred at $(0.5, 0.5, \sqrt{0.5})$ with radius 0.4.

18

Figure 17: Sphere with region of continuous conductivity. *Top left*: at time 0, *Top right*: at time 1.5. *Bottom left*: at time 2.3, *Bottom right*: at time 2.7.
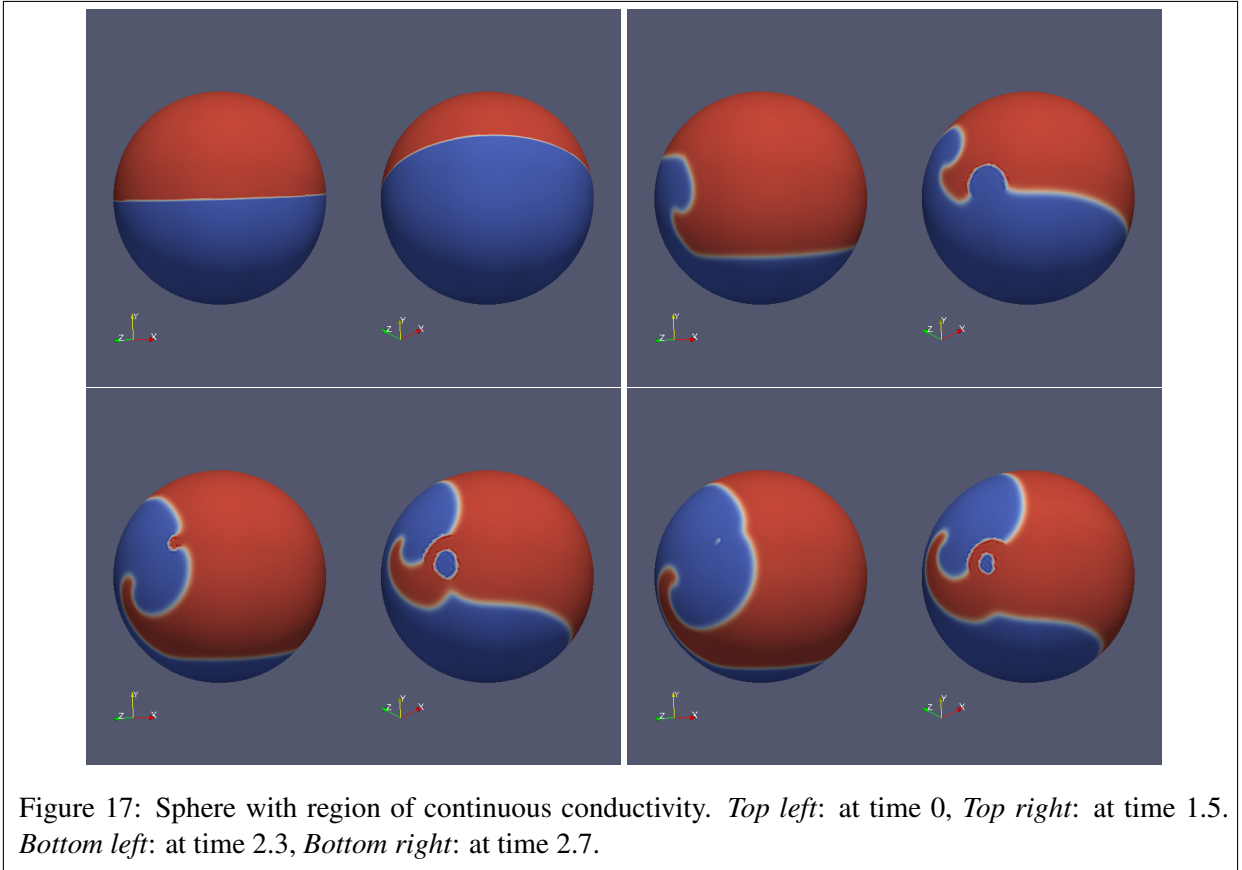
Refer to Figure 20 to see a graphic of the holes and the initial conditions.

The results of running the Barkley model on these domains is shown below in Figures 21, 22 and 23, with the two experiments displayed side-by-side with hole A on the left.

Figure 18: (continued) Sphere with region of continuous conductivity. *Top left*: at time 3.9, *Top right*: at time 5.5. *Bottom left*: at time 7.5, *Bottom right*: at time 8.3.

Figure 19: (continued) Sphere with region of continuous conductivity. *Left*: at time 9.2, *Right*: at time 13.9

Figure 20: Initial conditions on sphere with holes. *Left*: sphere with hole A. *Right*: sphere with hole B.
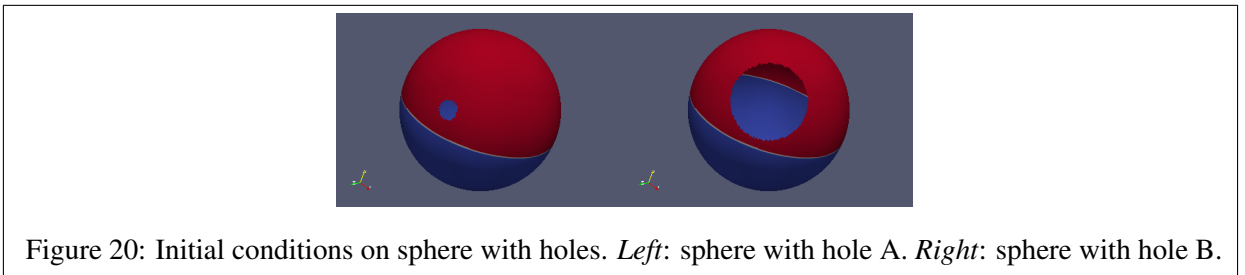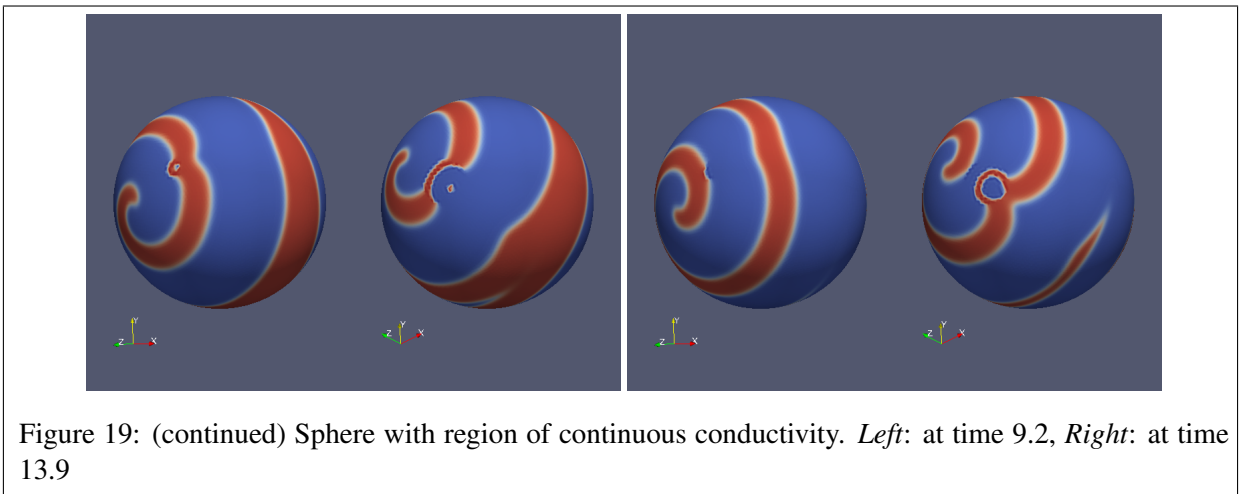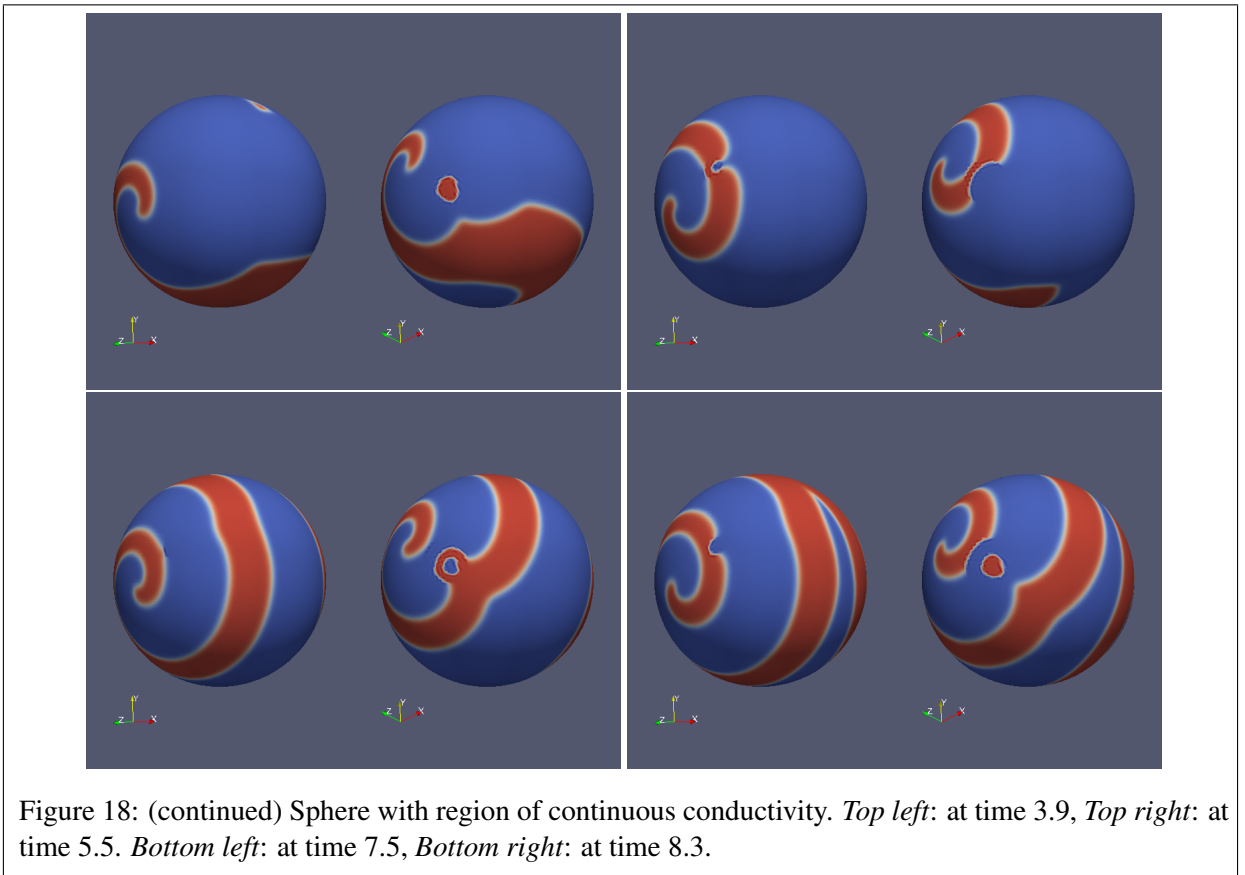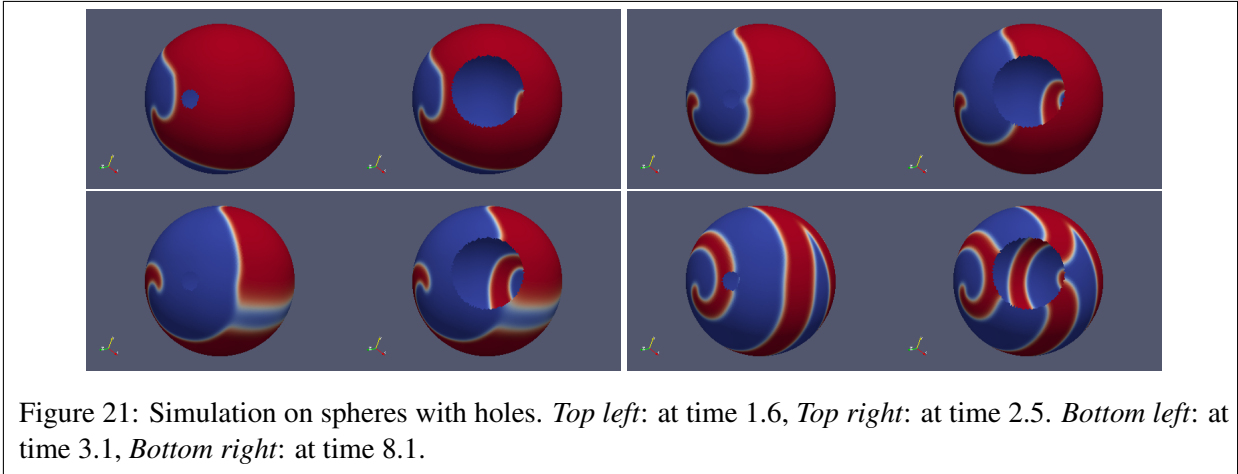
Figure 21: Simulation on spheres with holes. *Top left*: at time 1.6, *Top right*: at time 2.5. *Bottom left*: at time 3.1, *Bottom right*: at time 8.1.
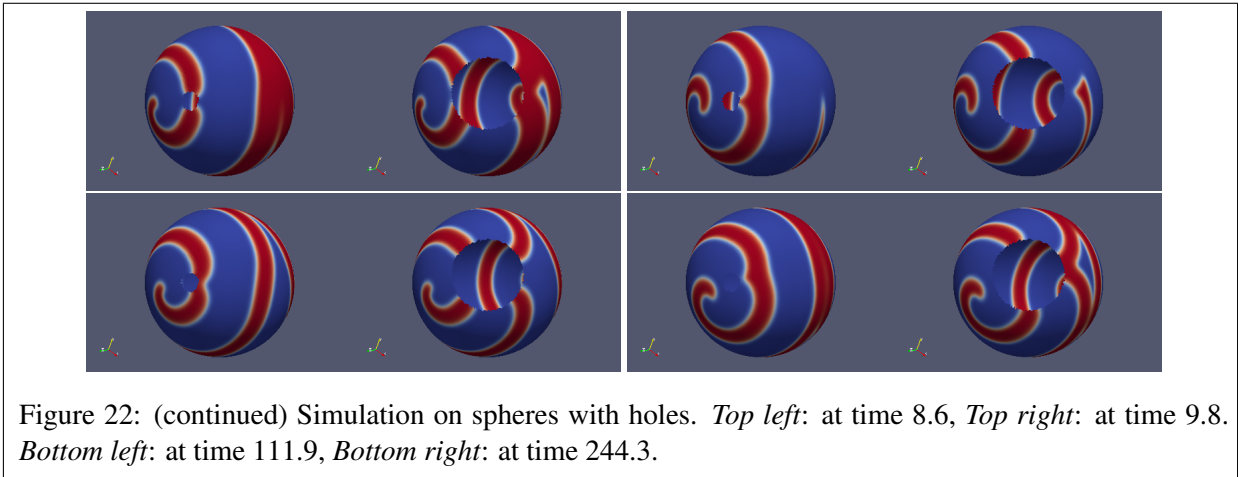
Figure 22: (continued) Simulation on spheres with holes. *Top left*: at time 8.6, *Top right*: at time 9.8. *Bottom left*: at time 111.9, *Bottom right*: at time 244.3.
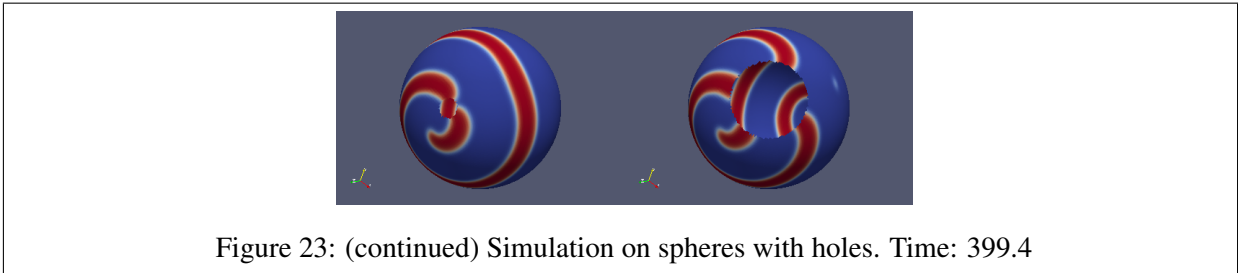
Figure 23: (continued) Simulation on spheres with holes. Time: 399.4

Analysis One can see from the outset that the holes have a pinching effect on the travelling waves, which appears more dramatic for the larger hole. This is the expected behaviour since the waves have an impenetrable barrier ahead of them so they must slow down and travel around the holes.

Comparing the final graphic (Figure 23, which is almost 400 seconds into the simulation) with the first figure, one can notice that the tip of the spiral has moved closer to the hole. This is called spiral *locking* in the literature. As the name suggests, the idea is that the centre of the spiral will eventually reside in the hole — unfortunately we do not have the computer resources to see this ourselves.

21

5 Moving Surfaces

5.1 Moving Sphere

Deformation   To make the model more realistic, we need to add movement to the surface. Starting with a unit sphere with the same initial conditions as in the fixed sphere case (see the start of Section 4), we apply a deformation along the y-axis of the form

$$1 + \alpha \sin\left(2\pi\beta t\right) \tag{12}$$

where t is time, $\alpha \in [-1, 1]$ is the scale of the deformation and β defines the period of the oscillation.

Clearly we cannot choose α to be greater in absolute value than 1 since this will lead to a collapse of the sphere (because then (12) can become negative). We also want α to be sufficiently large so that the movement is noticeable. We consider a range of different values of α fulfilling these conditions: 0.1, 0.2, 0.3, 0.4, 0.5.

Justification of choice of results   We also need to carefully select the period of oscillation. If it is too long (i.e., when β is restrictively small) then we need to have a long simulation to see any effects and this is computationally expensive. If the period is too short then we have numerical instabilities arising from the fact that the period is short compared to the timestep τ. We start by fixing $\beta = 0.1$ (which means that the period of one oscillation is 10 time-units). We run the simulation for 5 time periods; i.e., a total of 50 time units.

Choosing the correct time points to review our results is important. Obviously if we choose once a period we will be unable to see the oscillation. We decide to take the result at the end of the period for all five periods, the mid-point of the first period, and at the points with the maximum and minimum deformation in the first period. We also take two time images during the first time period, the reason for this is explained below. A animation of the whole period can be found at [2].
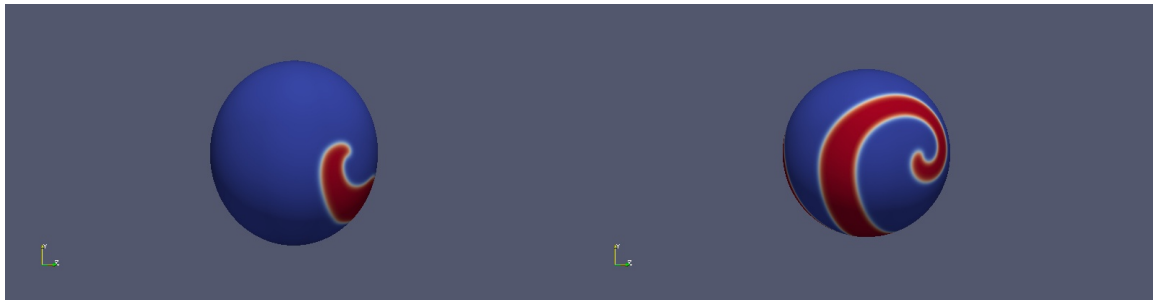
For each deformation we show the deformed sphere at the times 1.5, 1.95, 2.5, 5, 7.5, 10, 20, 30, 40, 50. Obviously the multiples of 10 are just the end of the periods, multiples of 5 are half-way through the first period and multiples of 2.5 and 7.5 are the times of maximum deformation of the sphere.
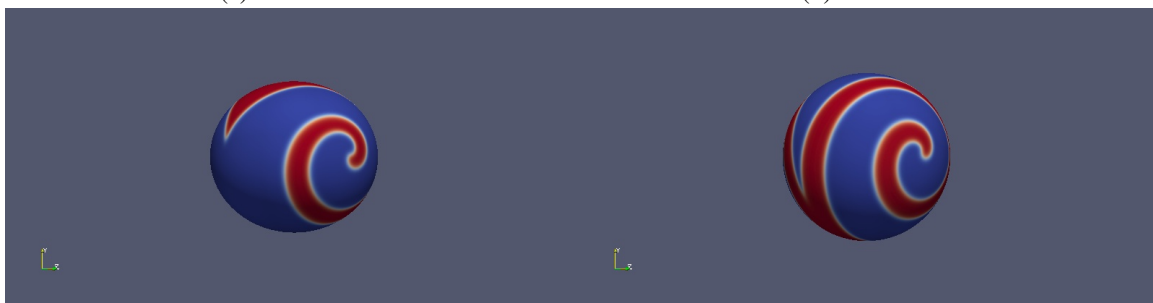
5.1.1 Deformation with $\alpha = 0.1$
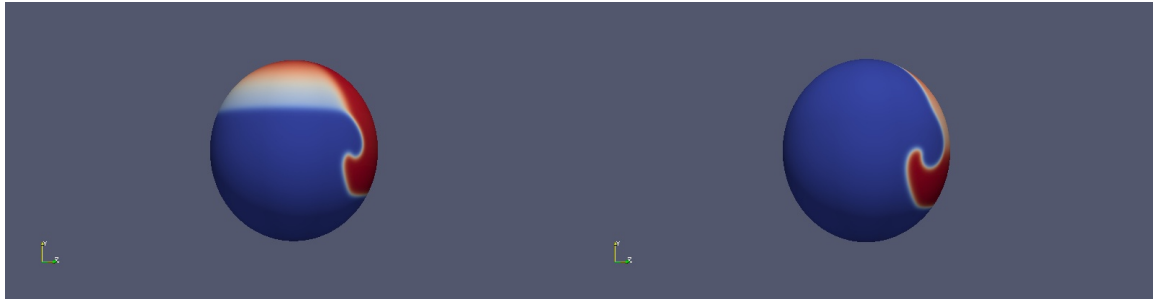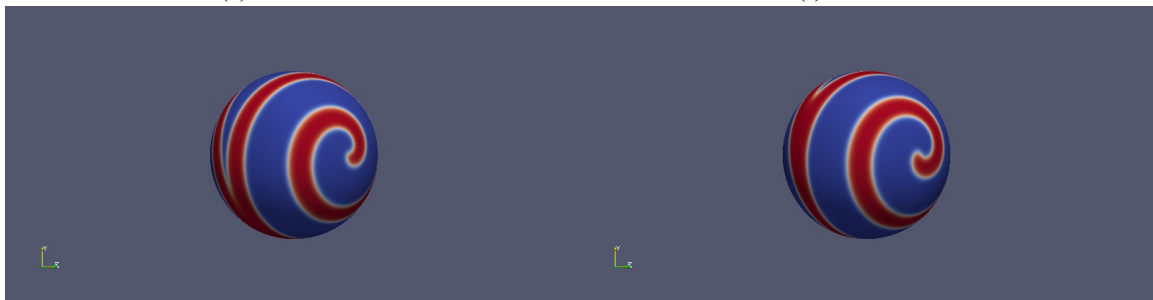

(a) Time: 1.5
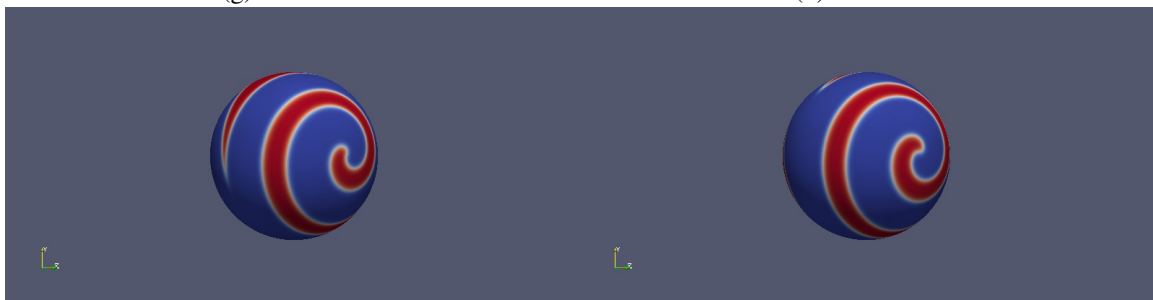
(b) Time: 1.95

(c) Time: 2.5

(d) Time: 5

(e) Time: 7.5
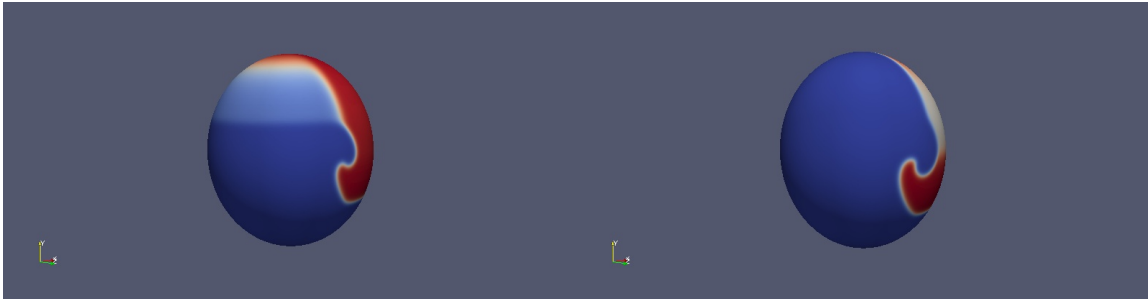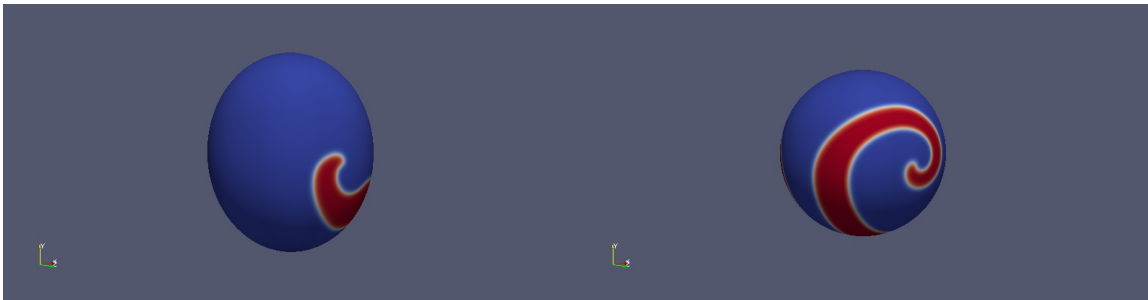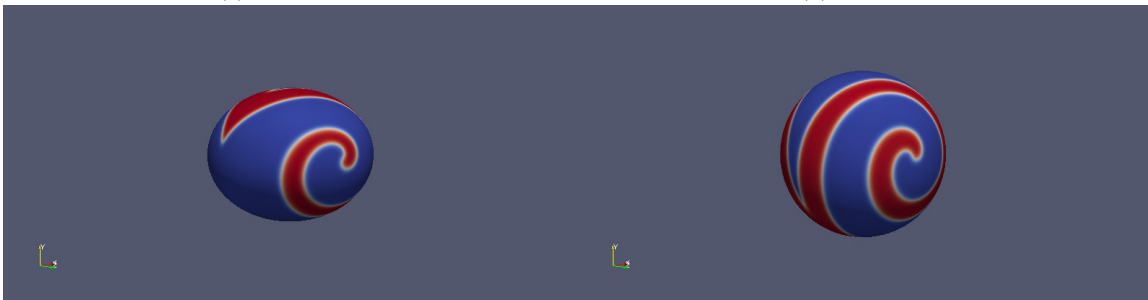
(f) Time: 10

(g) Time: 20

(h) Time: 30

(i) Time: 40

(j) Time: 50

5.1.2 Deformation with $\alpha = 0.2$

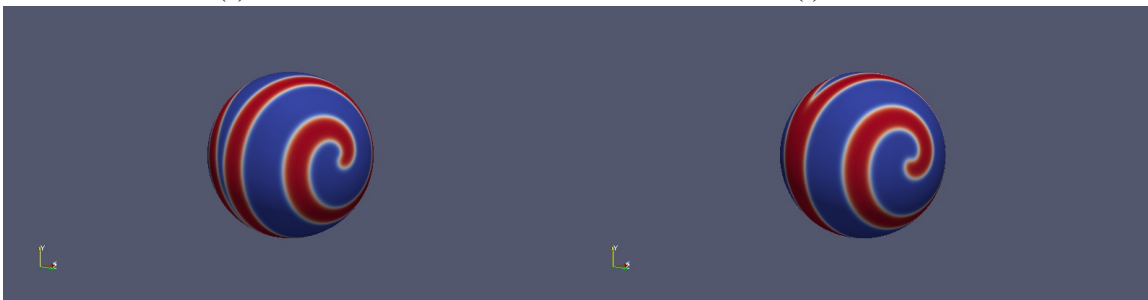(a) Time: 1.5

(b) Time: 1.95

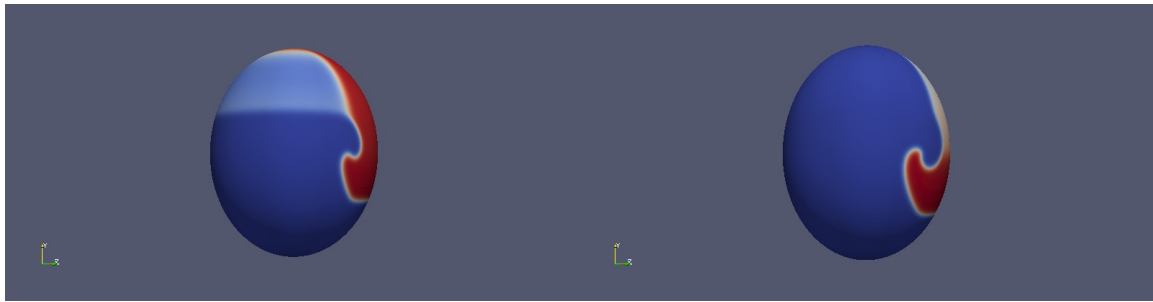(c) Time: 2.5

(d) Time: 5

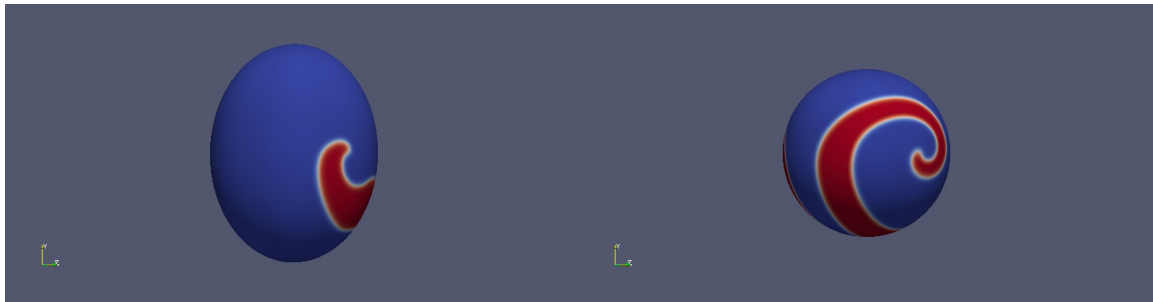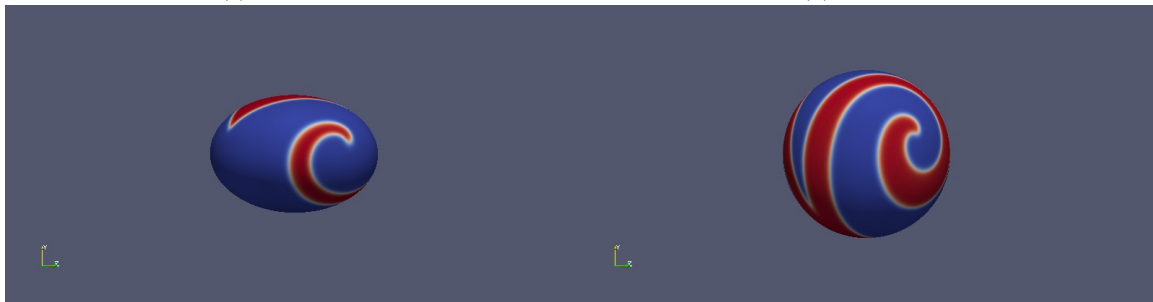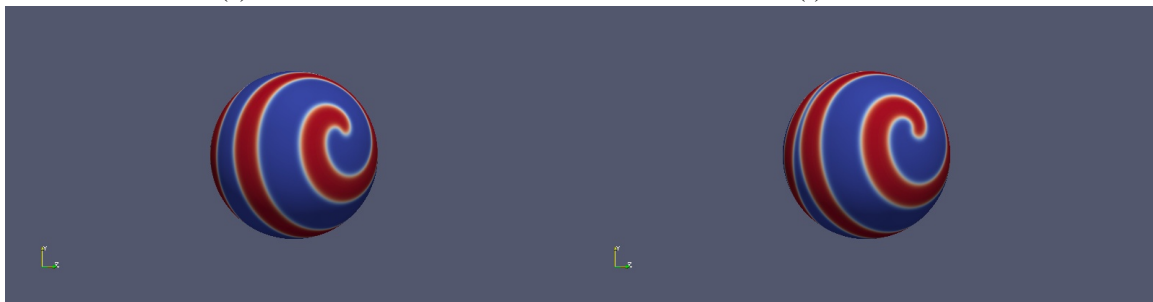(e) Time: 7.5

(f) Time: 10

(g) Time: 20

(h) Time: 30

5.1.3 Deformation with $\alpha = 0.3$

(a) Time: 1.5

(b) Time: 1.95

(c) Time: 2.5

(d) Time: 5

(e) Time: 7.5

(f) Time: 10

(g) Time: 20

(h) Time: 30

(i) Time: 40

(j) Time: 50

25

5.1.4 Deformation with $\alpha = 0.4$

(a) Time: 1.5

(b) Time: 1.95
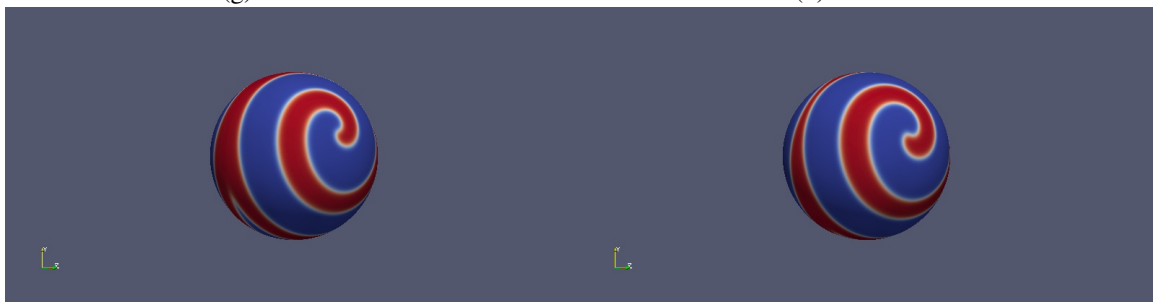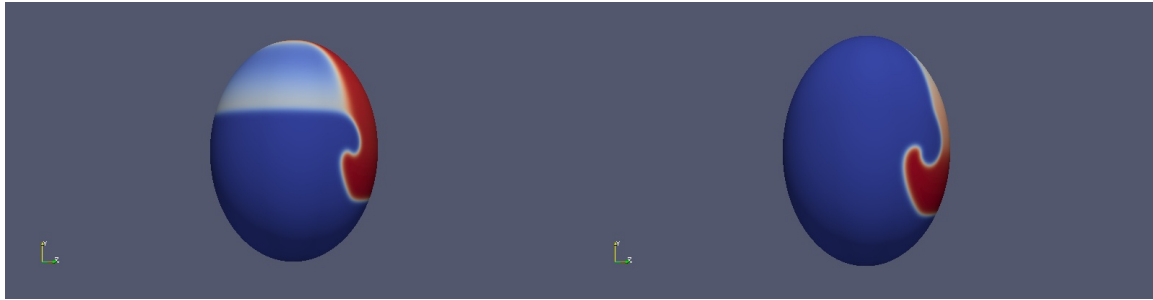
(c) Time: 2.5

(d) Time: 5

(e) Time: 7.5

(f) Time: 10

(g) Time: 20

(h) Time: 30

(i) Time: 40

(j) Time: 50

5.1.5 Deformation with $\alpha = 0.5$

(a) Time: 1.5

(b) Time: 1.95

(c) Time: 2.5

(d) Time: 5

(e) Time: 7.5
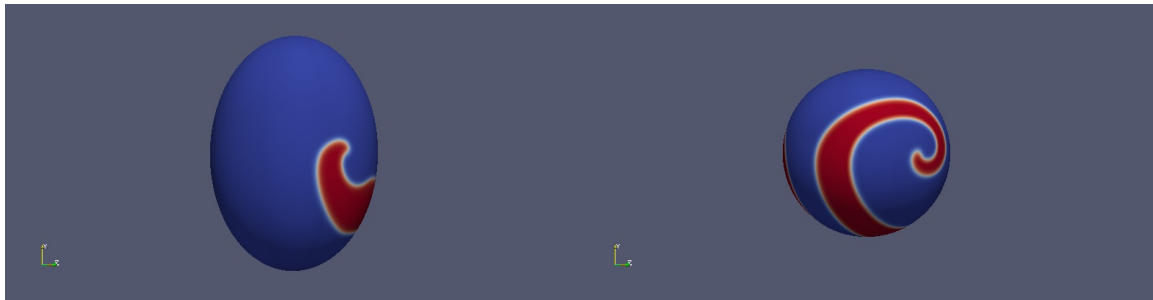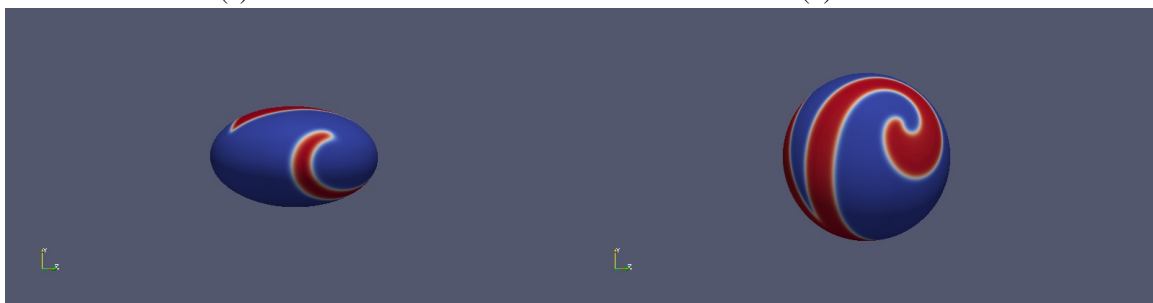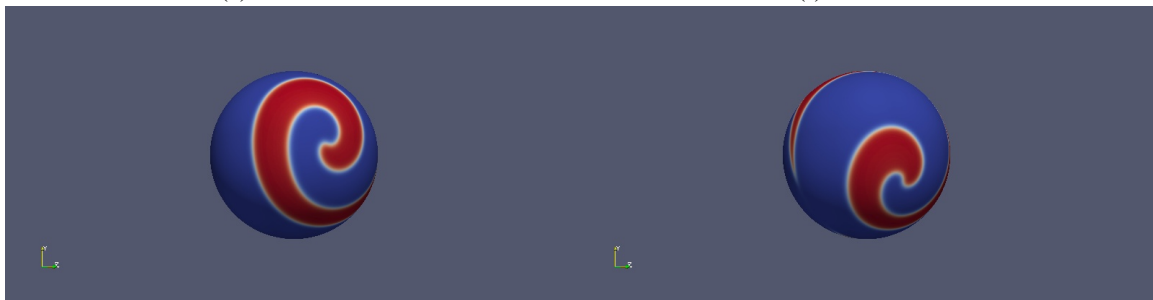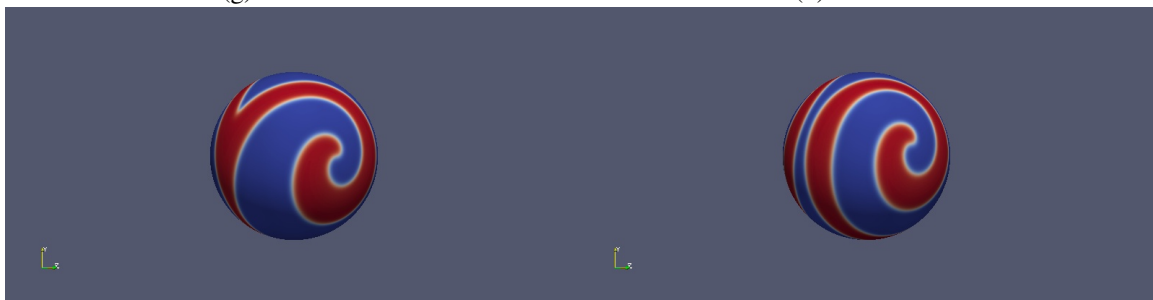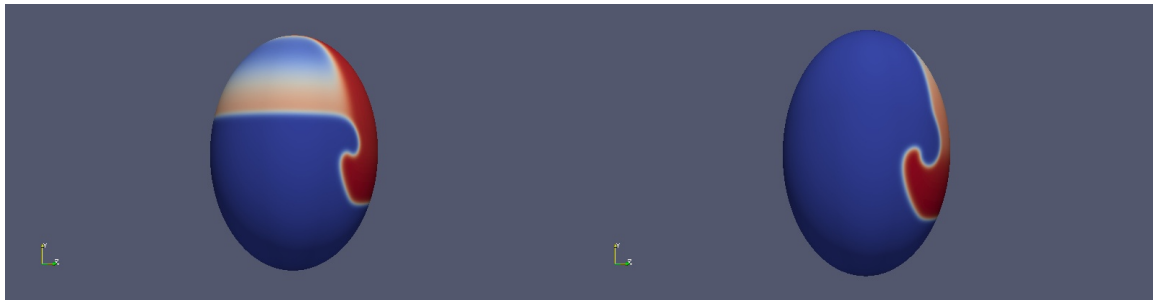
(f) Time: 10

(g) Time: 20

(h) Time: 30
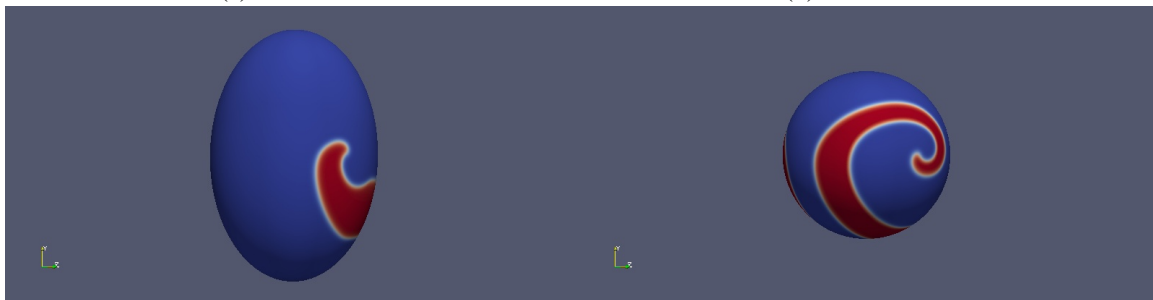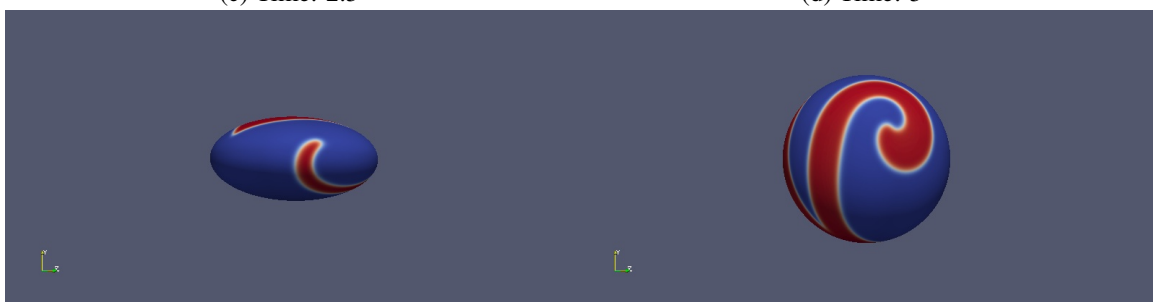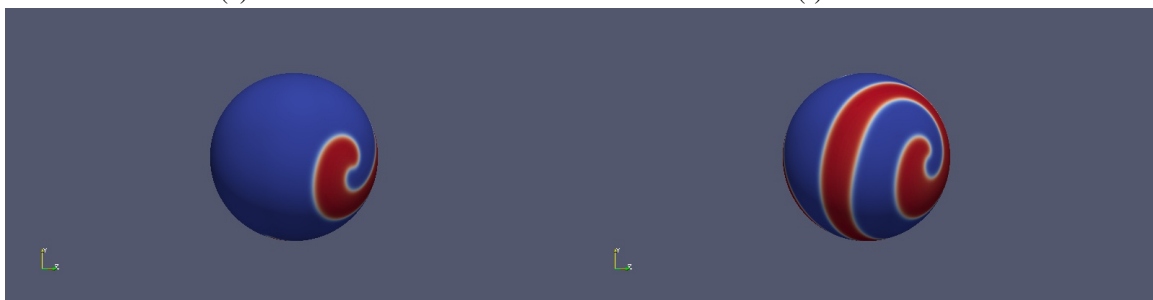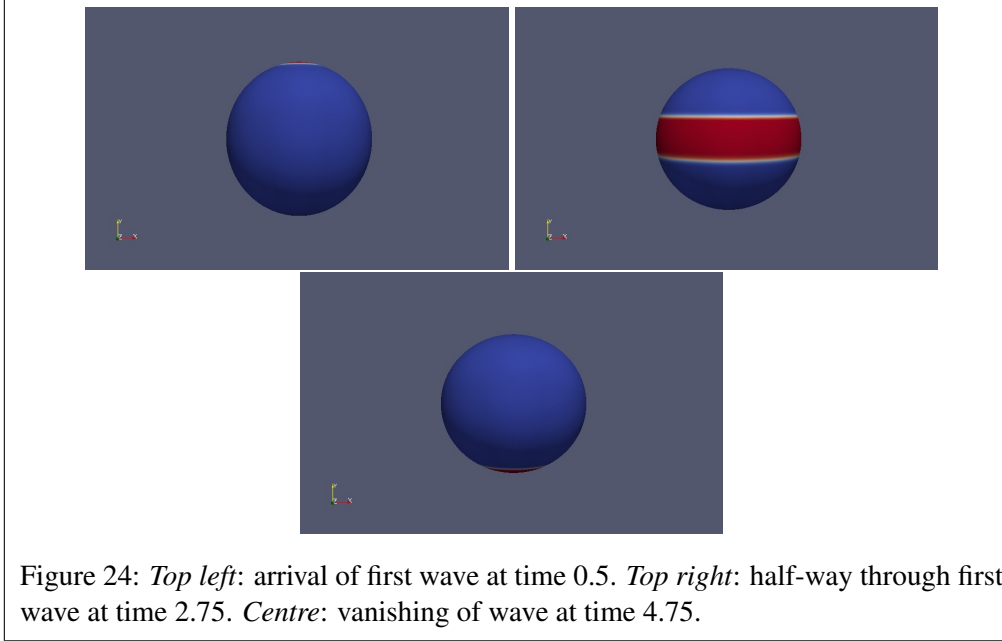
(i) Time: 40

(j) Time: 50

27

Figure 24: *Top left*: arrival of first wave at time 0.5. *Top right*: half-way through first wave at time 2.75. *Centre*: vanishing of wave at time 4.75.
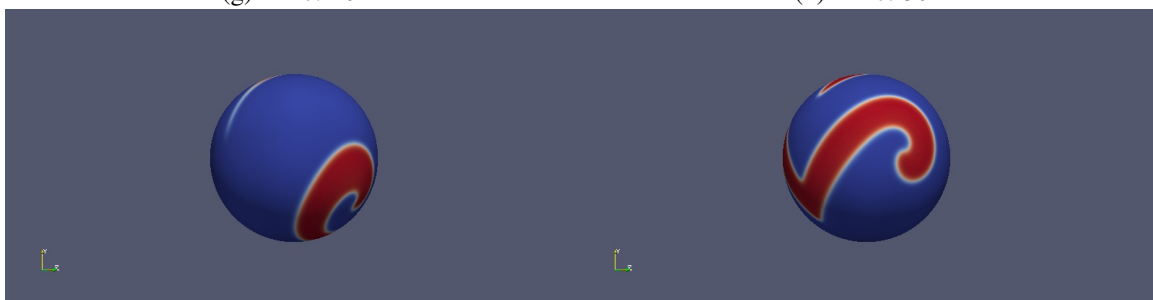
Analysis

We can see that in all deformations we successfully generate spirals. Also in contrast to the case of the static sphere we get a sudden reduction of the solution at the time points 1.5 and 1.95 for all cases. We can also see that the wave-form of the solution is deformed dramatically when the sphere is at its most deformed. Finally we can see by looking at the final time period that the centre of the spiral is moved by the deformation, this is especially prominent between the $\alpha = 0.4$ and $\alpha = 0.5$ deformation.

5.2   Pulse on Moving Sphere

We now demonstrate another aspect of how the Barkley model is physically relevant. To do this, we change the initial conditions to

$$u_0 = v_0 = 0$$

and add

$$(1 - u)\, \mathbb{I}_{y>0.95} \cdot \mathbb{I}_{u<0.99} \cdot \mathbb{I}_{\mathbb{Z} \leq t \leq \mathbb{Z}+0.05}$$

to the right hand side of (1). Here, the function $\mathbb{I}_{\mathbb{Z} \leq t \leq \mathbb{Z}+0.05}(t)$ equals 1 if $t \in [n, n + 0.05]$ for some $n \in \mathbb{Z}$ and equals zero otherwise. This allows us to observe a pulse passing from one side of the oscillating sphere to another.

Following the work from above, we oscillate the sphere by a factor of 1.1 along the y-axis with a period of 10 time units.

To create a wave, we need to alter u. To do this, every time unit, we have an impulse that occurs every time unit and lasts 0.05 time units. The impulse is confined to the region $y > 0.95$ of the sphere and the impulse only occurs if the previous wave is almost extinguished (i.e., $u < 0.99$). This is similar to the action potential in the heart when the pulse travels from one side to the other.

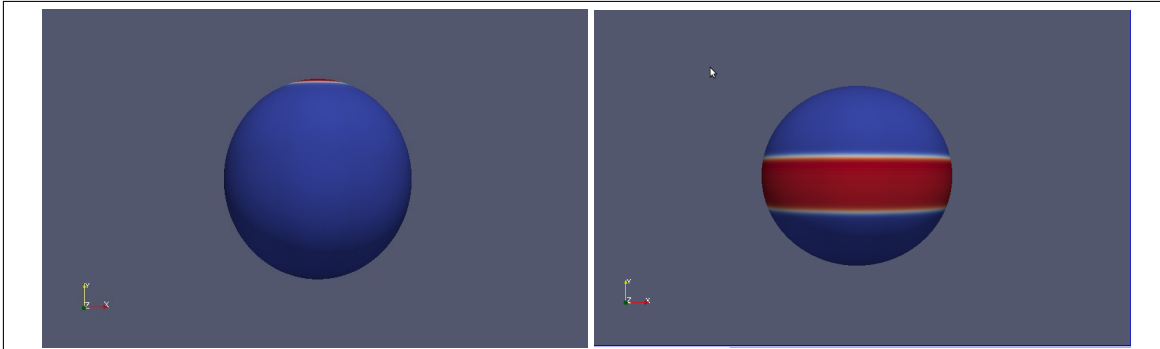See Figures 24 and 25 for the first and second occurrences of the wave.

Figure 25: *Left*: arrival of second wave at time 5.5. *Right*: half-way through second wave at time 7.5.

6 Closing Remarks

We set out to provide a framework in which to run simulations of the Barkley model on surfaces that can model the behaviour of spiral waves in the heart. Furthermore, we formulated and carried out simulations on surfaces with inhomogeneities and on moving surfaces. This showed interesting behaviour such as the tendency of the spiral waves to move towards inhomogeneities — such behaviour is known to occur on flat surfaces but accounts of our version on the spherical surface is less well-established in the literature.

Whilst we were successful in the sense that we wanted to provide a method for conducting simulations on non-trivial surfaces, there is, however, still plenty of work that would we like to have completed had we had more time.

Table 1 sums up what we have accomplished and what remains to be done. We discuss some of these and others below.

Stability   From the table we can see that one direction of possible further research is to fix the instability problems in various simulations; for example the implementation of thinner spirals, i.e., larger diffusion coefficient a.

Period of oscillations   Another example is to simulate a faster oscillating rate of the moving surface because the current rate 0.2π is a bit too low.

Parameter testing   For our simulations to truly model the heart accurately, we need to set the parameters of the Barkley model correctly so that they reflect the properties of the heart. This would require the study of biological data and collaboration with experts in the field.

Different spiral wave equations   In the heart, spiral waves often break up to create a turbulent environment. The results above suggest that our current model is very stable (we see no breakup even with very large oscillations). Thus we suggest altering the equations so that breakup is achieved. To do this, we change the source term g (following [6]) to

$$g(u,v) = u^3 - v.$$

This is still linear in v so the numerical methods are exactly the same, however the relation between v and u is more complicated. On a static sphere we need to alter both the parameters and the initial

Surface Γ	Diffusion coefficient a	Inhomogeneity	Method	Result
Ω_{150}	1	None	FD	Stable
$\Omega_{3.5}$	1/1790.49	None	FD	Stable
$\Omega_{3.5}$	1/179.049	None	FD	Stable
$\Omega_{3.5}$	1/1790.49	None	FE	Unstable
$\Omega_{3.5}$	1/179.049	None	FE	Stable
Unit sphere	1/179.049	None	FE	Stable
Unit sphere	1/1790.49	None	FE	Unstable
Unit sphere	2/1790.49	None	FE	Unstable
Unit sphere	1/500	None	FE	Unstable
Unit sphere	1/350	None	FE	Unstable
Unit sphere	1/250	None	FE	Unstable
Ellipsoid	1/179.049	None	FE	Stable
Unit sphere	1/179.049	Zero conductivity	FE	Unstable
Unit sphere	1/179.049	Reduced conductivity 1 (see (10))	FE	Stable
Unit sphere	1/179.049	Reduced conductivity 2 (see (11))	FE	Unstable
Unit sphere	1/179.049	Continuous conductivity	FE	Stable
Unit sphere	1/179.049	Physical hole	FE	Stable
Moving surface $(0.1, 2)$	1/179.049	None	FE	Unstable
Moving surface $(0.01, 2)$	1/179.049	None	FE	Unstable
Moving surface $(0.1, 0.2)$	1/179.049	None	FE	Stable
Moving surface $(0.1, 0.4)$	1/179.049	None	FE	Unstable
Moving surface $(0.2, 0.2)$	1/179.049	None	FE	Stable
Moving surface $(0.3, 0.2)$	1/179.049	None	FE	Stable
Moving surface $(0.4, 0.2)$	1/179.049	None	FE	Stable
Moving surface $(0.5, 0.2)$	1/179.049	None	FE	Stable
Moving surface	1/179.049	Any type	FE	TODO
Fixed heart geometry	Any	Physical holes and damaged tissues	FE	TODO
Pulsating heart geometry	Any	Physical holes and damaged tissues	FE	TODO

Table 1: The results of experiments done and list of experiments to be done in further research. The (α, β) next to "Moving surface" in the first column means the scale of deformation is α and the rate β (see (12)).
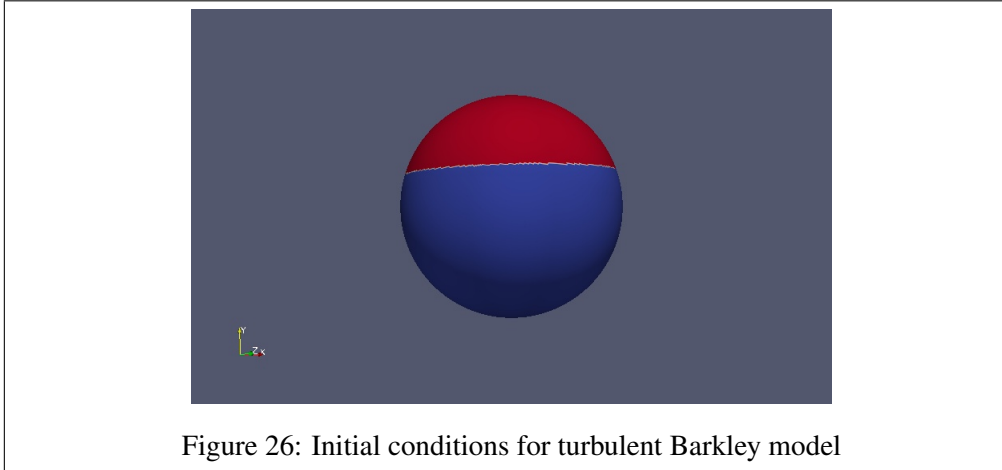
conditions. Our parameters become

$$a = \frac{1}{179.049}, \qquad b = 0.06, \qquad c = 0.75, \qquad \epsilon = 0.06$$

and our initial conditions are

$$u(x, y) = \mathbb{I}_{y > 0.3}$$
$$v(x, y) = \frac{3}{8}\mathbb{I}_{x > 0},$$

See Figure 26 for a graphic. Although the initial stages before forming a spiral are different, in the

Figure 26: Initial conditions for turbulent Barkley model

end we still end up with the same spiral waves (see Figure 27) that we witnessed in Section 4. Our attempts to simulate this turbulent regime on an oscillating sphere gave us numerical instability and unfortunately we did not have enough time to run the simulation with a higher level of time refinement.

Figure 27: Spiral wave on the sphere
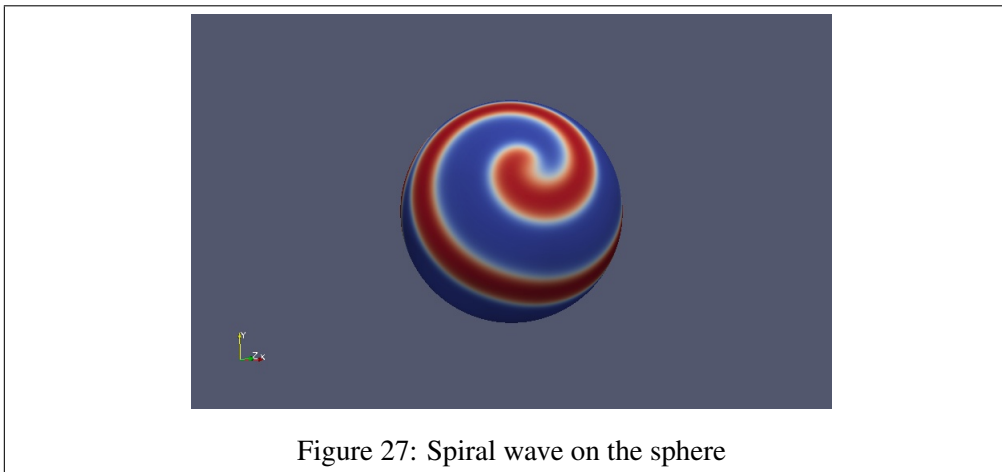
Other experiments Simulating the equation on a more realistic heart-shaped geometry would be better; for example see [12, p. 79]. Also, applying the inhomogeneities we formulated above to moving surfaces would be a natural first progression. This would be slightly harder to achieve because the domain is moving but it is certainly possible.

References

[1] Relevant heart anatomy and physiology. `https://wiki.engr.illinois.edu/display/BIOE414/Relevant+Heart+Anatomy+and+Physiology`. [Online; accessed 7 May 2012].

[2] A. Alphonse, S. Bignold and Y. Pei. Media and motion webpage. `http://www2.warwick.ac.uk/fac/sci/masdoc/current/msc-modules/ma916/media_and_motion`, May 2012.

[3] A. Dedner, R. Klöfkorn, M. Nolte and M. Ohlberger. A Generic Interface for Parallel and Adaptive Scientific Computing: Abstraction Principles and the DUNE-FEM Module. *Computing*, 90(3–4):165–196, 2010.

[4] A. Dedner, R. Klöfkorn, M. Nolte and M. Ohlberger. DUNE-FEM Web page, 2011. http://dune.mathematik.uni-freiburg.de.

[5] D. Barkley. A model for fast computer simulation of waves in excitable media. *Physica D, 49 ,p61-70*, 1991.

[6] D. Barkley. `http://www.scholarpedia.org/article/Barkley_model`, 2008. [Online; accessed 8 May 2012].

[7] M. Blatt and P. Bastian. The iterative solver template library. In Bo Kågström, Erik Elmroth, Jack Dongarra, and Jerzy Waśniewski, editors, *Applied Parallel Computing. State of the Art in Scientific Computing*, volume 4699 of *Lecture Notes in Computer Science*, pages 666–675. Springer, 2007.

[8] G. Dziuk and C. Elliott. Finite elements on evolving surfaces. *IMA Journal of Numerical Analysis,27 ,p262-292*, 2007.

[9] J. Gomatam and F. Amdjadi. Reaction-diffusion equations on a sphere: Meandering of spiral waves. *Phys Rev E, 56 ,4 p3913-3919*, 1997.

[10] R. Kapral and K. Showalter. *Chemical Waves and Patterns*. Understanding Chemical Reactivity, Vol. 10. 1994.

[11] M. Alhajri, T. Colledge and A. Kister. Research proposal: Media and motion. *Unpublished*, 2012.

[12] L. Mirabella. Numerical methods for cardiovascular problems: computational electrocardiology and fluid dynamics in moving domains . *Ph.D thesis, Politecnico di Milano* , 2010.

[13] P. Bastian, M. Blatt, A. Dedner, C. Engwer, R. Klöfkorn, M. Ohlberger and O. Sander. A generic grid interface for parallel and adaptive scientific computing. part I: Abstract framework. *Computing*, 82(2–3):103–119, 2008.

[14] P. Bastian, M. Blatt, A. Dedner, C. Engwer, R. Klöfkorn, M. Ohlberger, O. Sander, J. Fahlke, C. Gräser and M. Nolte. DUNE Web page, 2011. http://www.dune-project.org.

[15] P. Bastian, M. Blatt, A. Dedner, C. Engwer, R. Klöfkorn, M. Ohlberger, R. Kornhuber and O. Sander. A generic grid interface for parallel and adaptive scientific computing. part II: Implementation and tests in DUNE. *Computing*, 82(2–3):121–138, 2008.

[16] T. Shajan, S. Sinha and R. Pandit. Spiral-wave dynamics depends sensitively on inhomogenities in mathematical models of ventricular tissue. *Phys Rev E 011929*, 2007.

[17] Wikipedia. Basic cardiac action potential. `http://en.wikipedia.org/wiki/File:Action_potential2.svg`, August 2009. [Online; accessed 13 May 2012].